Investigating the *in vivo* Spatial Distribution of Hippocampal Microstructure and Macrostructure

Bradley G. Karat[1,2], Jordan DeKraker[1,3], Uzair Hussain[4], Stefan Köhler[5], Ali R. Khan[1,6]

[1]Robarts Research Institute, Schulich School of Medicine and Dentistry, University of Western Ontario, Canada, [2]Neuroscience Graduate Program, University of Western Ontario, Canada, [3]Montreal Neurological Institute, McGill University, Montreal, Quebec, Canada, [4]University Health Network, Toronto, Ontario, Canada, [5]Department of Psychology, University of Western Ontario, Canada, [6]Western Institute for Neuroscience, University of Western Ontario, Canada,

Abstract

The hippocampus is classically divided into mesoscopic subfields which contain varying microstructure that contribute to their unique functional roles. It has been challenging to characterize this microstructure with current MR based neuroimaging techniques. In this work, we used a novel surface-based approach in the hippocampus to show distinct microstructural distributions of myelin, neurite density and dispersion, fractional anisotropy, and mean diffusivity using diffusion MRI. To get at this issue we used the Neurite Orientation Dispersion and Density Imaging (NODDI) model optimized for gray matter diffusivity and diffusion tensor imaging (DTI). We found that neurite dispersion was highest in the Cornu Ammonis (CA) 1 and subiculum subfields which likely captures the large heterogeneity of tangential and radial fibers, such as the Schaffer collaterals, perforant path, and pyramidal neurites. Neurite density and myelin content were highest in the subiculum and lowest in CA1, which may reflect known myeloarchitecture differences between these subfields. We show macrostructural measures of gyrification, thickness, and curvature which were in line with *ex vivo* descriptions of hippocampal anatomy. We employed a multivariate orthogonal projective non-negative matrix factorization (OPNNMF) approach to capture co-varying regions of macro- and microstructure across the hippocampus. The clusters were highly variable along the medial-lateral (proximal-distal) direction, which is expected as there are known differences in morphology, cytoarchitectonic profiles, and connectivity. Long-axis (anterior-posterior) differences can also be seen in the OPNNMF components, where the body of the hippocampus has more parcellations than the head and tail. Finally, we show that by examining the main direction of diffusion relative to canonical hippocampal axes, we could identify microstructure that may map onto specific tangential fiber pathways, such as the Schaffer collaterals and perforant path. These results highlight the value of combining *in vivo* diffusion MRI with computational approaches for capturing hippocampal microstructure, which may provide useful features for understanding cognition and for diagnosis of disease states.

Keywords: Hippocampus; Subfields; Microstructure; Neurite Density; Neurite Dispersion; Diffusion MRI

1. Introduction

The hippocampus is classically divided into mesoscopic subfields according to differences in cyto-, myelo-, and chemoarchitecture defining structurally distinct units (Duvernoy et al., 2013; Ding & Van Hoesen, 2015). The neurites and fiber pathway circuitry that compose the microstructure of the hippocampus exist within and across the subfields. For example, the pyramidal neurites that exist within the Cornu Ammonis (CA) and subiculum subfields have apical and basal dendrites which project across the layers or laminae, while their axons project to the alveus, a major white matter bundle adjoining the hippocampus. The trisynaptic pathway is the major circuitry component which connects the subfields of the hippocampus. The entorhinal cortex connects to the dentate gyrus (DG) and other subfields through the perforant path. The DG then projects to the pyramidal neurites of CA3 through the mossy fibers, which then project to CA1 through the Schaffer collaterals. Finally, CA1 projects to the subiculum and back to the entorhinal cortex as the main hippocampal outflow. Hippocampal microstructure is key in producing unique cognitive functions such as memory formation and storage and spatial navigation among others (Voss et al., 2017; Goodroe et al., 2018; Horner et al., 2015). Furthermore, the hippocampus is typically one of the earliest aberrant structures in many disease states where specific microstructural properties are differentially afflicted or spared (Moodley & Chan, 2014; Dhikav & Anand, 2012; Small et al., 2011). While much work has addressed volumetric characterization of the hippocampus, understanding hippocampal microstructure can provide key insights into its complex cognitive functions as well as its early deterioration in disease.

Diffusion magnetic resonance imaging (dMRI) is a particular technique which holds promise in probing the hippocampal circuitry by sensitizing the measured MRI signal to the movement of water molecules, which diffuse more readily parallel to microstructure. Several models have been proposed that attribute measures of the dMRI signal to compartments which have varying diffusivity environments (Assaf et al., 2008; Assaf & Basser, 2005; Zhang et al.,

2012). One of the earliest and most widely used models proposed by Basser et al. (1994) is diffusion tensor imaging (DTI). DTI estimates quantitative parameters such as fractional anisotropy (FA - a measure of the restriction of diffusion), mean diffusivity (MD), and the ellipsoidal orientation of the diffusion process. However, DTI has some notable limitations. At increasing b-values (approximately greater than 1000-1500 s/mm^2) there is contribution from multiple compartments with varying diffusivities (such as restricted intracellular water), which is beyond the monoexponential decay assumptions of DTI (Assaf & Cohen. 2000). As well, regions of crossing fibers result in planar DTI ellipsoids with understated FA values (Campbell et al., 2005). Furthermore, DTI measures are sensitive to multiple microstructural properties at the same time, decreasing its specificity (Pierpaoli et al., 1996). Newer models aim to utilize the dependence of the diffusion signal attenuation to varying sets of biophysically motivated compartments.

One of the most popular compartmental models is Neurite Orientation Dispersion and Density Imaging (NODDI), which aims to provide a biophysical interpretation of the diffusion signal (Zhang et al., 2012). NODDI assumes that three microstructural environments consisting of an intra-cellular, extra-cellular, and cerebrospinal fluid (CSF) compartment contribute to the diffusion signal. The intracellular compartment is modeled as a set of infinitely anisotropic sticks (diffusion can only be parallel to the main orientation of the stick), while the extracellular compartment is modeled as a zeppelin with hindered diffusion perpendicular to its main axis. The CSF compartment is modeled as a sphere with gaussian isotropic diffusion. Diffusion is assumed to be contained separately within each compartment, where the resulting signal is the sum of all compartments. NODDI aims to overcome the limitations of DTI by providing microstructural scalars such as the neurite density index (NDI) and orientation dispersion index (ODI) which are sensitive to fiber crossings and are biophysically grounded (Zhang et al., 2012).

Extant work has attempted to examine hippocampal microstructure with DTI and NODDI. Some such studies have found age-related deterioration of hippocampal microstructure by

averaging NODDI measures within subfields (Radhakrishnan et al., 2020) while others have shown regionally specific deterioration using DTI (Yassa et al., 2010). Another study investigated the variation of DTI and intracortical myelin across the hippocampus using non-negative matrix factorization, however, they did not make quantitative comparisons of microstructure within and across the subfields (Patel et al., 2020). A recent cortical study examined the distribution of NODDI metrics and cortical thickness across the entire cerebral cortex including the hippocampus by averaging metrics across all subjects within each cortical parcel (Fukutomi et al., 2018). Thus, they only examined coarse-grained averages across the entire hippocampal volume. The distributions of NODDI and DTI measures have not been extensively investigated within the hippocampal subfields and across its longitudinal axis.

The orientation and trajectory of the hippocampal circuitry including the trisynaptic circuit has been probed previously using tractography and polarized light imaging (PLI). *Ex-vivo* work has indeed resolved all or part of the hippocampal circuitry using dMRI tractography (Beaujoin et al., 2018) and PLI (Zeineh et al., 2017) in a small number of samples. While these studies serve as ground-truth references for the orientation of hippocampal circuitry, a difficult step has been recapitulation of this circuitry *in-vivo*, which is critical for characterization of variability associated with healthy and disease states. Some *in-vivo* work has attempted to use DTI to capture parts of the trisynaptic circuit such as the perforant path (Yassa et al., 2010) or the whole hippocampal circuitry (Zeineh et al., 2012). However, it is unclear whether the found trajectories are anatomically valid. Furthermore, at lower resolutions, tracts can be spurious requiring complex acquisition and correction schemes, and since acquisitions can vary across studies, tractography practically always requires separate optimization of its parameters (Zeineh et al., 2012). Improved understanding of hippocampal microstructure *in-vivo* requires granular investigation of metrics derived from common models like NODDI and DTI within and across the subfields, as well as characterization of the main orientation of the microstructure that is used for tractography.

In the current study, we examined the spatial distribution of NODDI and DTI metrics, intracortical myelin, and macrostructural features of thickness, gyrification, and curvature across the hippocampus using high-resolution *in vivo* human connectome project (HCP) data (Van Essen et al., 2013). Furthermore, we use Orthogonal Projective Non-Negative Matrix Factorization (OPNNMF) as a multivariate approach to capture regions of the hippocampus where these metrics co-vary. We aimed to compare the current OPNNMF representation to previous work which has looked to examine the dimensions of hippocampal organization along its medial-lateral (across subfields) and anterior-posterior (longitudinal) axes (Genon et al., 2021; Robinson et al., 2015; Zhong et al., 2019; Cheng et al., 2020; Plachti et al., 2019; Plachti et al., 2020; Patel et al., 2020, DeKraker et al., 2020). We utilized a novel surface-based subfield segmentation approach called *HippUnfold* (DeKraker et al., 2018; DeKraker et al., 2021a). The goal of surface-based alignment is to project hippocampi to a 2D flat/unfolded surface. Using a surface-based approach can account for interindividual differences in tissue curvature and digitation across the whole anterior-posterior extent of the hippocampus (DeKraker et al., 2021b). Hippocampi in unfolded space are aligned based on topology and the contiguity of subfields, allowing unprecedented anatomical detail. Finally, hippocampal gray matter shows a laminar distribution similar to that of other cortical areas with large radial and tangential neurite components, although the highly curved structure of the hippocampus is reflected in the complexity of its neurite orientations. Importantly, these neurite orientations tend to be highly aligned along one of the axes of the hippocampus that span the anterior-posterior (AP longitudinal), proximal-distal (PD - across subfields), or inner-outer (across laminae) directions (Figure 1A and B). *HippUnfold* provides a coordinate system along these three axes. Thus, we also aimed to determine if the known stereotyped orientations of microstructure

can be elucidated by analyzing their primary orientation along each of the axes *in vivo*, as depicted in Figure 1B.

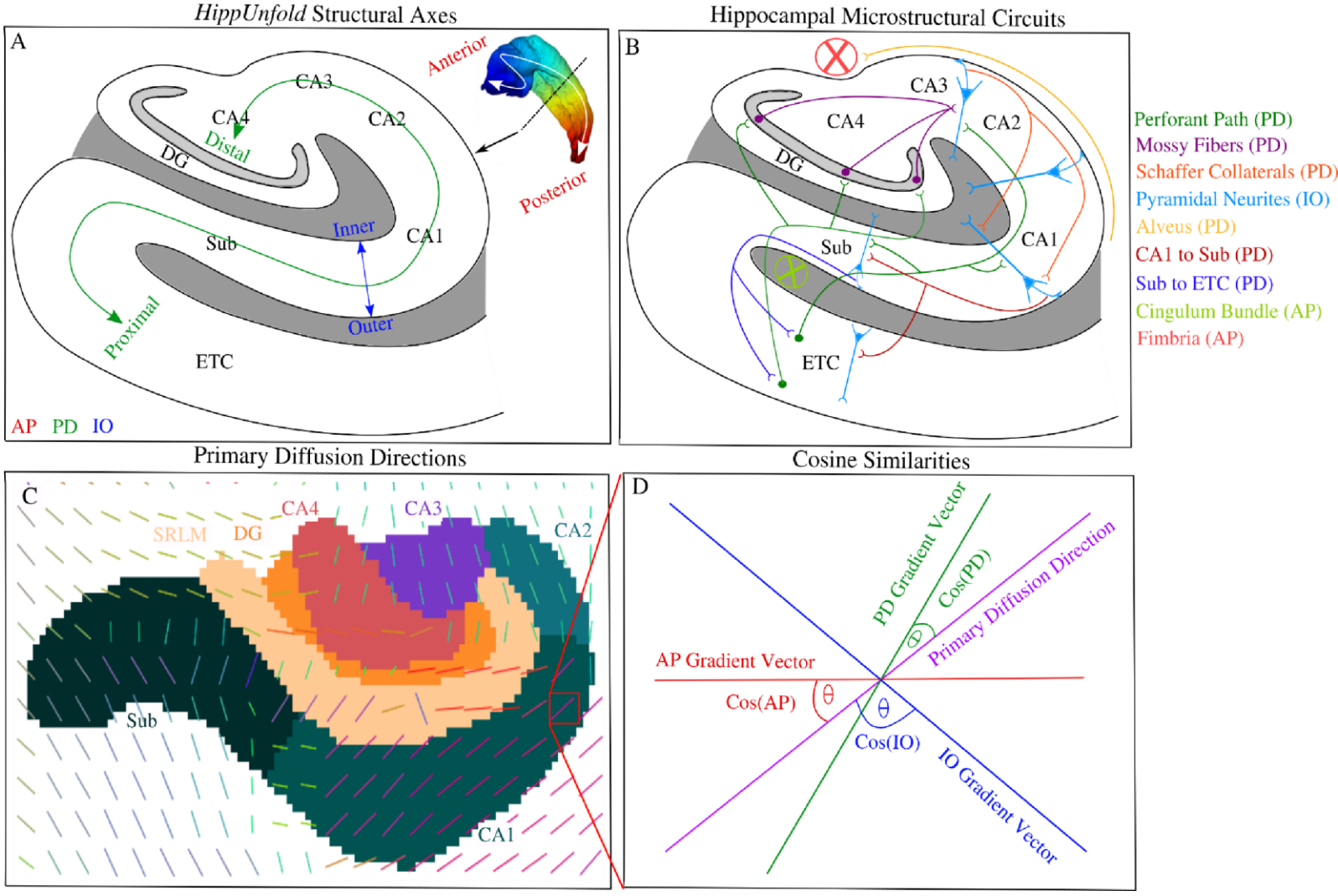

Figure 1. Depicting hippocampal structural axes, the stereotyped organization of microstructure, and diffusion vectors of the hippocampus. (A) A coronal slice depicting the structural axes of the hippocampus defined as anterior-posterior (AP), proximal-distal (PD), and inner-outer (IO) provided by *HippUnfold*. (B) Known microstructural circuits within the hippocampus and their main orientation relative to the hippocampus, defined by the colour coded legend on the right. (C) Primary diffusion directions for one subject (μ of the watson distribution from NODDI) overlaid on a coronal slice of hippocampal subfields provided by *HippUnfold*. (D) Pictorial example representing the NODDI and hippocampal axis vectors in a single voxel defined in (C). Cosine similarities are represented as the angle between the NODDI vector and each hippocampal vector,

providing a measure of orientation coherence along each cardinal axis (see *2.5)*. Sub - Subiculum, CA - Cornu Ammonis, DG - Dentate Gyrus, SRLM - Stratum Radiatum Lacunosum Moleculare, ETC - Entorhinal Cortex.

2. Methods

2.1 Overview

A subset of 100 unrelated subjects from the publicly available Human Connectome Project (HCP) 1200 dataset were used for this study (Van Essen et al., 2013). All 100 subjects were run through *HippUnfold* (DeKraker et al., 2021a), a new automated tool for surface-based subfield segmentation and hippocampal unfolding (see *2.3*; DeKraker et al., 2018). The coordinates generated from *HippUnfold* within each subject were used to calculate vector fields along each main axis of the hippocampus (see *2.3 &* Figure 1A*)*. NODDI and DTI metrics were calculated in each subject's native space using whole-brain diffusion images (see *2.2* and *2.4*). Cosine similarities between the NODDI orientational vector (defined as μ of the Watson distribution see *2.4*) and the vectors along each of the 3 axes (AP, PD, and IO) were calculated at each voxel. Macrostructural measures of curvature, gyrification, and thickness were calculated along the midthickness surface (middle of the hippocampal gray matter) of the hippocampus across all subjects (see *2.6)*. NODDI measures of ODI and NDI, DTI measures of FA and MD, and the cosine similarities were all sampled along the midthickness surface within each subject and averaged in unfolded space (DeKraker et al., 2018). Plots of NODDI and DTI metrics, cosine similarities, and macrostructure metrics across the midthickness surface were visualized as folded and unfolded surfaces. Finally, Orthogonal Projective Non-Negative Matrix Factorization (OPNNMF) was used to capture co-varying regions of the hippocampus and to examine the dimensions of macro- and microstructure hippocampal organization.

2.2 Data acquisition and preprocessing

We used the publicly available HCP young adult dataset (ages 22-35), which consisted of structural and diffusion MRI data for 1200 subjects (Van Essen et al., 2013). To avoid any biases caused by family structures, we chose the 100 unrelated subjects subset for analysis (mean age: 27.52 years +/- 3.47 years; F/M: 54/46). Data included T1-weighted (T1w) and T2-weighted (T2w) structural images at 0.7 mm^3 isotropic resolution and diffusion-weighted data at 1.25 mm^3 isotropic resolution. Structural images were obtained using a 3D MPRAGE sequence (TR-2400ms, TE–2.14ms, TI-1000ms, FOV-224x224 mm). Diffusion images were obtained using a spin-echo echo-planar sequence (b=0 (18 acquisitions), 1000, 2000, 3000s/mm^2, 90 diffusion-encoding directions, TR-5520ms, TE-89.5ms, FOV-210x180mm). Data used in the preparation of this work were obtained from the Human Connectome Project (HCP) database (Van Essen et al., 2013). In this work we utilized the preprocessed structural and diffusion images for the HCP dataset. Preprocessing of structural images included: gradient distortion correction, coregistration and averaging of repeated T1w and T2w runs using 6-DOF rigid transformation, initial brain extractions for T1w and T2w, field map distortion correction and registration of T2w with T1w images, bias field correction, and atlas registration. Preprocessing of diffusion images included: intensity normalization across runs, EPI distortion correction, eddy current and motion correction, gradient nonlinearity correction, and registration of the mean b0 image to T1w native space. The full pre-processing pipeline for structural and diffusion images were published elsewhere (Andersson et al., 2015; Glasser et al., 2013; Jenkinson et al., 2002; Sotiropoulos et al., 2013) and can be found at the HCP website

(https://www.humanconnectome.org/study/hcp-young-adult). Myelin maps were calculated by dividing the T1w image intensity by the T2w image intensity and correcting for the bias field (Glasser & Van Essen, 2011; Glasser et al., 2014), which is referred to as myelin for the rest of the

paper. It should be noted that the T1w over T2w image ratio is thought to be sensitive to myelin but is an indirect measure.

2.3 HippUnfold - Hippocampal Unfolding and surface-based segmentation

The newly developed *HippUnfold* (DeKraker et al., 2021a) tool was used in the current study. The general steps of *HippUnfold* are: 1) preprocess and resample T2w images to a cropped subvolume at 0.3mm^3 isotropic resolution for the left and right hemispheres, 2) automatically segment hippocampal gray matter tissue via a custom model trained with nnUNet, a generalizable implementation of a neural network U-Net architecture (Isensee et al., 2020), 3) post-processing via fluid-label registration to a topologically averaged template, 4) impose coordinates by solving Laplace's equation along the AP, PD, and IO axes, 5) extract gray matter macrostructural features such as curvature, gyrification, and thickness along the midthickness surface which is defined by Laplacian coordinates (see *2.6*), 6) generate transformations from native to unfolded space using the Laplace coordinates and scattered interpolation, and finally, 7) apply subfield boundaries according to predefined topological coordinates from an unfolded high-resolution ground-truth atlas (DeKraker et al., 2020). Due to the small size of the Dentate Gyrus (DG) and CA4, we combined them into a single DG/CA4 subfield label. As well, most of the DG is excluded in our surface representation. All subfield segmentations for both hemispheres were reviewed for gross errors by BK. The midthickness surfaces used in this study were composed of 2004 vertices with a spacing of roughly 1mm. Each vertex is inherently aligned across subjects in unfolded space since the generation of the Laplace coordinates used the same topological boundaries. Thus, this implicit topological registration allows for the averaging of metrics across subjects at each vertex.

2.4 Characterization of microstructure with NODDI & DTI

NODDI models the diffusion signal as a combination from 3 microstructural environments: intracellular, extracellular, and cerebrospinal fluid (CSF) (Zhang et al., 2012). The intracellular compartment is considered the space that is bounded by neurites, which is modelled as a set of

sticks. The stick geometry captures the restricted diffusion of water perpendicular to neurites, and the relatively unhindered diffusion along them. Furthermore, sticks can capture the wide range of neurite orientations, from highly coherent to highly dispersed tissue. The extracellular compartment is the space around the neurites, which consists of glial cells and in gray matter, the somas. In extracellular space, the signal is modeled as Gaussian anisotropic diffusion to represent the hindered but not restricted movement of water. Finally, the CSF compartment is modelled as Gaussian isotropic diffusion, representing the free movement of water. NODDI does not draw any *a priori* assumptions about whether a voxel is gray matter, white matter or CSF, and thus it treats each voxel as a possible combination of different compartments (Zhang et al., 2012). Thus, the normalized dMRI signal can be written as:

$$E_{NODDI} = f_{iso}E_{iso}(d_{iso}) + W(\mu,\kappa)[f_{ec}E_{ec}(d_{perp}, d_{par}) + f_{ic}E_{ic}(d_{par})] \quad (1)$$

Where $f_{iso}E_{iso}, f_{ec}E_{ec}$ and $f_{ic}E_{iC}$ are the volume and signal fractions of the CSF, extracellular, and intracellular (NDI) compartments, respectively. The extracellular and intracellular compartments are linked orientationally by the Watson distribution $W(\mu,\kappa)$, where κ is the concentration parameter (ODI $= \frac{2}{\pi}\arctan(\frac{1}{\kappa})$) and μ is the mean orientation of the Watson distribution (herein referred to as the NODDI microstructural vector or primary diffusion direction). The hindered perpendicular diffusion of the extracellular compartment d_{perp} is set via a tortuosity model. The original NODDI model developed mainly for white matter sets the parallel diffusivity value d_{par} equal to $1.7 \times 10^{-3}\frac{mm^2}{s}$ and the isotropic or CSF compartment diffusion to $3.0 \times 10^{-3}\frac{mm^2}{s}$. Previous studies in the gray matter have sought to optimize d_{par}, and have consistently found that the lowest mean squared error is achieved with d_{par} equal to $1.1 \times 10^{-3}\frac{mm^2}{s}$ (Guerrero et al., 2019; Fukutomi et al., 2018). Thus, in the current study we used the gray matter optimized d_{par} value of $1.1 \times 10^{-3}\frac{mm^2}{s}$ for fitting the NODDI model. The Microstructure Diffusion Toolbox

(MDT; Harms et al., 2017) was utilized to fit the NODDI model using whole-brain diffusion images aligned to their respective T1w space with all b-values (b=0, 1000, 2000, 3000 s/mm2). MDT can fit models using Maximum Likelihood Estimation to get a point estimate on all parameters or Markov Chain Monte Carlo sampling to recover the full posterior distribution of model parameters. The validity of the assumptions of the NODDI model are discussed in section 4.8.

We also used the MDT (Harms et al., 2017) to calculate metrics of FA and MD using DTI. DTI was performed using only the $b = 1000\ \frac{s}{mm^2}$ volumes to align with typical DTI experiments (Behrens & Johansen-Berg, 2014). Both the NODDI and DTI metrics were mapped onto the hippocampal midthickness surface using the process described below.

We used Connectome Workbench (https://github.com/Washington-University/workbench) to sample values at each surface vertex from voxel data. In this study we used 2004 vertices defined along the midthickness surface of the hippocampus to reduce partial volume effects. To sample voxel data along the midthickness surface we used a ribbon-constrained mapping algorithm which also requires the inner and outer surfaces also generated by *HippUnfold.* The ribbon method constructs a polyhedron from the vertex's neighbor on each surface defined, and then estimates the volume of the polyhedron that falls inside any nearby voxels to use as weights. We further reduced the weight of any particular voxel based on its distance from the midthickness surface, where the scaling value was calculated using a Gaussian with a standard deviation (sigma) determined by the cortical thickness at each vertex. This has the effect of more aggressively down-weighting voxels further from the midthickness surface where the hippocampus is thinner. We then averaged each metric at each vertex across all subjects to generate the average maps which were plotted in folded and unfolded space.

2.5 Examining the primary direction of diffusion relative to hippocampal axes

Analyses were performed to attempt to capture the stereotyped orientation of hippocampal microstructure which tends to be highly aligned along the AP, PD, and IO axes. We obtained vector fields along the AP, PD, and IO axes by taking the first derivative of the respective Laplacian coordinates provided by *HippUnfold* (Figure 1A), such that the vectors only pointed along one of the axes. This was done within cropped subvolumes for each subject separately for the left and right hemispheres. The result was 3 distinct vector images within a hemisphere for each subject and axis. The NODDI microstructural vectors were rotated to the same cropped subvolume space from their native T1w space. We then calculated cosine similarities between the generated vectors along the AP, PD, and IO axes and the NODDI microstructural vector at each voxel (Figure 1C & D). All vectors were normalized before calculating cosine similarities. The cosine similarity was defined as the inner product between vectors:

$$abs\left(\frac{\bar{a}\cdot\bar{u}}{|\bar{a}|\,|\bar{u}|}\right) \quad (2)$$

Where $\bar{a}$ was a hippocampal axis vector in a single voxel (AP, PD, or IO), and $\bar{u}$ was the NODDI microstructural vector (μ of the Watson distribution) at the same voxel. We constrained the range of cosine similarity values to be between 0 and 1 (representing angles of 90 degrees to 0 degrees between vectors, respectively) since the vectors cross each other in each voxel.

All cosine similarities were calculated in an upsampled (0.3 mm^3) subject-specific cropped subvolume space in each hemisphere. There were a total of 3 cosine similarity images (one for AP, PD, and IO similarity values) within each hemisphere for each subject. Each scalar cosine similarity image was sampled along the midthickness surface. In the topologically aligned unfolded space, we averaged cosine similarities across all subjects for the left and right hemispheres separately.

2.6 Correlations between all metrics

Correlations were performed at the level of the vertex averaged maps. Pearson's R correlation between all metrics were calculated using vertices averaged across all participants (Figure 2C-J average maps) and across both left and right hemispheres. Before removing outliers, there were 2004 averaged vertices to be correlated between any two metrics. Outlier values were removed by identifying vertices that were +- 3 standard deviations away from their respective metrics mean. Since these correlations were mainly exploratory, we did not report a single cut-off alpha value to be used to determine significance.

2.7 Orthogonal Projective NNMF (OPNNMF)

Orthogonal Projective NNMF (OPNNMF) was used in this work to attempt to identify co-varying regions in the hippocampus using the metrics described above (Sotiras et al., 2015; Yang & Oja, 2010). OPNNMF decomposes an input matrix X of dimensions a x b into a component matrix C (a x k) and a weight matrix W (k x b). The number of components (k) is defined *a priori*. The component and weight matrices are derived such that their multiplication best reconstructs the input data (X ~ C x W). OPNNMF solves the following minimization problem to estimate C (Sotiras et al., 2015):

$$\|X - CC^TX\|^2 \text{ subject to } C \geq 0, C^TC = I, \text{and } W = C^TX \quad (3)$$

Where $||\ ||^2$ represents the squared Frobenius norm and I denotes the identity matrix which enforces orthogonality among C. C is first initialized using a non-negative double singular value decomposition (Boutsidis & Gallopoulos, 2008). Then, C is updated through an iterative process until it converges on an optimal solution. The iterative multiplicative update rule is as reported by Yang and Oja (2010):

$$\grave{C}_{ij} = C_{ij} \frac{(XX^TC)_{ij}}{(CC^TXX^TC)_{ij}} \quad (4)$$

Where i represents the number of vertices and j represents the number of components. The component matrix C represents the latent structure in the data and allows for an examination of the underlying covariance in multivariate data. As done in Patel et al. (2020) the sparse and non-overlapping component matrix allows for each vertex to be assigned an output component using a winner take all method which improves the interpretability of the spatial output components. The weight matrix W represents the subject-metric coefficients, allowing for an examination of subject-specific and metric-specific contributions to each component.

2.8 Implementing OPNNMF

A total of 11 metrics were included in the OPNNMF implementation (ODI, NDI, myelin, FA, MD, gyrification, thickness, curvature, AP cosine similarity, PD cosine similarity, IO cosine similarity) with subsets of these metrics used for more specific analyses (i.e. NODDI only, DTI only, macrostructure only, and cosine similarity only). The input matrix X was built using all 2004 vertices of the midthickness surface in unfolded space for all 11 metrics across all 100 subjects per hemisphere. That is, each subject contributed 11 unfolded space maps to the input matrix. Thus, the input matrix had 1100 columns (100 subjects x 11 metrics - defined as subject-metrics) and 2004 rows (2004 vertices) for a single hemisphere. Normalization was required since the metrics had varying magnitudes. First, each metric was z-scored within each hemisphere. Then, each z-scored metric distribution was shifted by the minimum value from all the z-scored metrics to ensure all metrics were on the same scale and there were no negative values. All distributions were manually inspected to ensure the minimum value used was not an outlier.

OPNNMF was implemented using publicly available and open MATLAB code at https://github.com/asotiras/brainparts (Sotiras et al., 2015; Yang & Oja, 2010; Boutsidis & Gallopoulos, 2008; Halko et al., 2011). OPNNMF was run with a max number of iterations = 10000, tolerance = 0.00001, and non-negative double singular value decomposition initialization.

2.9 Stability & Reconstruction Error

The quantification of OPNNMF decomposition stability followed that of Patel et al. (2020). Stability was assessed by examining the similarity of the spatial component matrix C across varying splits of data. All 100 subjects were randomly split into two groups of equal sizes. OPNNMF was then performed on each split independently. A within-split similarity matrix was then derived by multiplying a particular splits component matrix by the transpose of itself (i.e. a cosine similarity). The result is a 2004x2004 (number of vertices x number of vertices) matrix where each row contains the cosine similarity of component scores between a vertex and all other vertices. Finally, a Pearson's correlation coefficient was calculated across the rows of the cosine similarity matrix between splits to quantify if the decomposition maintained the relationships between vertices. The above process was repeated 6 times, each with a new random split of the data. The mean and standard deviation of the correlation coefficient was taken across all vertices and splits for a given component solution. A correlation of 1 represented perfect stability (i.e. each split of the data had perfect correspondence between vertex relationships), whereas -1 represented instability. The above process was then repeated for different component decompositions, from k=2 to k=12. Reconstruction error was calculated through 3-steps. First, the component matrix C and the weight matrix W were estimated and then multiplied together to return the reconstructed input matrix. The original and reconstructed input matrix were then subtracted to obtain a reconstruction error matrix. The Frobenius norm of the reconstruction error matrix was then taken to get the reconstruction error. The gradient in the reconstruction error was taken across solutions with varying component numbers to assess the magnitude of the improvement in reconstruction error when adding more components.

2.10 Interpreting OPNNMF

The output component matrix C contains a component value for each vertex while the weight matrix W describes how each subject-metric is projected onto each component. A large value in

the component matrix can be interpreted as a particular vertex being identified as a part of the variance pattern. The weight matrix can be used to elucidate which metrics contributed to each component as well as inter-subject variance within metrics. In the current study these 2 matrices were used to explore spatial patterns and the contributions of particular metrics to each component. A winner-take-all method was used where a vertex was assigned the integer of the component with the highest component weighting value from the matrix C. The whole matrix W was plotted to examine metric-specific trends.

3. Results

The results begin with qualitative descriptions of average macro- and microstructural measures and their correlations on the midthickness hippocampal surface (middle of the hippocampal gray matter). We then present the cosine similarities between NODDI microstructure vectors and the hippocampal axis vectors. Finally, we present the OPNNMF results including the stability analysis and a 6-component solution.

3.1 Distributions of Hippocampal Metrics

Figure 2 presents Pearson's R correlations, mean macro- and microstructural metrics, along with subfield segmentations shown on an averaged hippocampal midthickness surface in folded and unfolded space. The standard deviation of these metrics is shown in supplementary Figure 1. The dispersion of neurites (ODI - Figure 2C) is highest in the anterior and middle parts of CA1 and the distal parts of the subiculum, while dispersion is lower in the middle and posterior of CA3 and CA2 and at the most proximal edge of the subiculum. Much like the neocortex, large radial and tangential components exist across the hippocampal subfields (Duvernoy et al., 2013). Tangential microstructure such as the Schaffer collaterals and most of the perforant path along with radial microstructure such as the pyramidal neurites all contribute to the high orientational heterogeneity seen in CA1 and the subiculum (Figure 1C), which likely drives the increased ODI seen there (see *4.1*). Neurite density (NDI - Figure 2D) is largest in the body and tail of the subiculum, while there

is lower neurite density in CA1. The low density in CA1 is likely a result of the large pyramidal cell layer with the pyramids themselves noted as being widely separated, compared to the higher density of neurites in CA2 and CA3 (Jürgen et al., 2011). Myelin has a strikingly similar distribution to that of NDI, as found in previous cortical studies (Figure 2E Fukutomi et al., 2018). Myelin, ODI, and NDI maps appear to strongly agree with subfield borders.

Macrostructure features of thickness, gyrification, and curvature are shown in Figure 2H-J. Gyrification is largest in anterior CA1 and the DG/CA4. The thickest regions are the anterior and posterior of the subiculum and CA1, as well as throughout the DG/CA4, while CA3 and CA2 are thin. Curvature tends to be highest in the anterior part of the subiculum, along the spine of the hippocampus (red arrows in Figure 2H), and in CA3. The macrostructural measures appear to vary greatly across the subfields (PD) and longitudinal (AP) axes. These findings are largely in line with previous work (DeKraker et al., 2020).

Correlations between these metrics can be seen below the diagonal in Figure 2A and will be described in the below sections.

3.2 Correlations between NODDI metrics & myelin

In Figure 2D and E, strong qualitative similarities can be seen between NDI and myelin. Both are high in the subiculum and CA3/CA2 regions, while hypointensities are noted in CA1. A strong positive correlation is seen between NDI and myelin ($R = 0.86$, $p < 0.0000001$, Figure 2A). Although, it has been shown previously that the hippocampal NDI and myelin do not follow the same relationship as other cortical areas after averaging across the whole hippocampal volume (low myelin with high NDI compared to rest of cortex Fukutomi et al., 2018). Here we show that a strong correlation still exists between the two when looking more granularly.

ODI (Figure 2C) and NDI (Figure 2D) are moderately to strongly correlated ($R = -0.31$, $p < 0.0000001$). This correlation has also been noted across the entire cortex (Fukutomi et al., 2018).

3.3 Correlations between NODDI & DTI metrics

Qualitatively, the map of FA (Figure 2F) closely resembles the inverse of the ODI map (Figure 2C) while also following the NDI map (Figure 2D). Particularly, the distinct pattern of high dispersion appears as low FA, while high neurite density appears as high FA. Furthermore, the map of MD (Figure 2G) generally resembles the inverse of the NDI map (Figure 2D). The border of CA2/CA1 has a distinctly low NDI which translates into an increased MD. ODI and FA are strongly correlated ($R = -0.85$, $p < 0.0000001$), and ODI and MD are weakly correlated ($R = -0.10$, $p < 0.0001$). Furthermore, NDI and FA are strongly correlated ($R = 0.67$, $p < 0.0000001$) and NDI and MD are moderately to strongly correlated ($R = -0.40$, $p < 0.0000001$).

A disentangling of FA as determined by ODI and NDI has been reported previously in cortical gray matter (Zhang et al., 2012). Two voxels with different neurite densities can have the same FA as long as the one with the larger neurite density also has the larger dispersion (Zhang et al., 2012). We report a similar level of disentangling within the hippocampus in supplementary Figure 2A.

3.4 Correlations between macrostructure and NODDI metrics

Thickness and NDI are moderately correlated ($R = -0.25$, $p < 0.00001$), thickness and ODI are not correlated ($R = 0.02$, $p = 0.5$), and thickness and myelin are moderately correlated ($R = -0.20$, $p < 0.00001$). From Figure 2 it can be noticed that in the subiculum (apart from its most anterior region) thickness is relatively low while NDI and myelin are high. Furthermore, along the anterior of the hippocampus across all subfields thickness tends to be high while NDI and myelin tend to be low. Thus, when thickness is increased in particular regions of the hippocampus, NDI and myelin tend to decrease.

Gyrification and NDI are moderately to strongly correlated ($R = -0.35$, $p < 0.000001$), gyrification and ODI are moderately correlated ($R = 0.21$, $p < 0.000001$), and gyrification and myelin are strongly correlated ($R = -0.48$, $p < 0.0000001$). Gyrification is largest in CA1 and the

DG/CA4, and lowest in the subiculum and CA2. Conversely, myelin and NDI are largest in the subiculum and lowest in CA1, resulting in a relatively strong negative correlation between the two.

Curvature and NDI are moderately correlated ($R = -0.27$, $p < 0.000001$), curvature and ODI are weakly correlated ($R = -0.15$, $p < 0.0001$), and curvature and myelin are moderately to strongly correlated ($R = -0.31$, $p < 0.0000001$). Interestingly, the highly curved spine of the hippocampus (Figure 2J - red arrows) appears to correspond to the large hypointense regions of myelin (Figure 2E) and NDI (Figure 2D), likely driving a large part of the noted correlations.

3.5 Examination of the primary direction of diffusion relative to hippocampal axes

This section qualitatively analyzes the mean of the cosine similarities (Figure 1D; Figure 3) between the hippocampal vectors along the anterior-posterior (AP), proximal-distal (PD), and inner-outer (IO) (Figure 1A) axes and the NODDI microstructural vectors along the midthickness surface (Figure 1C). Here we provide descriptions of microstructure (Figure 1B) that likely contribute to the orientation results.

Anterior-Posterior alignment: The high AP alignment in the body of the DG to CA3 is likely driven by the neighbouring fimbria, the largest bundle in that region oriented AP. High AP alignment in the subiculum is likely caused by the cingulum, a large fiber bundle that traverses the parahippocampal gyrus. Some partial voluming from the outer (where the cingulum exists) to the midthickness surface is expected, which may drive this alignment.

Proximal-Distal alignment: High PD alignment in the head of CA3 is expected to be either Schaffer collaterals which curve immediately PD off of the apical dendrites of the pyramidal cells or from perforant projections coming from the entorhinal cortex and entering CA3 which are also oriented PD. High PD alignment in CA1 is likely a result of the Schaffer collaterals. The Schaffer collaterals make synaptic contact at the apical and basal dendrites of CA1 in a PD fashion (Nieuwenhuys et al., 2008; Swanson et al., 1978). However, the perforant path could also

contribute to a higher PD alignment as it moves from the entorhinal cortex to the DG synapsing on CA1 along the way (Nieuwenhuys et al., 2008).

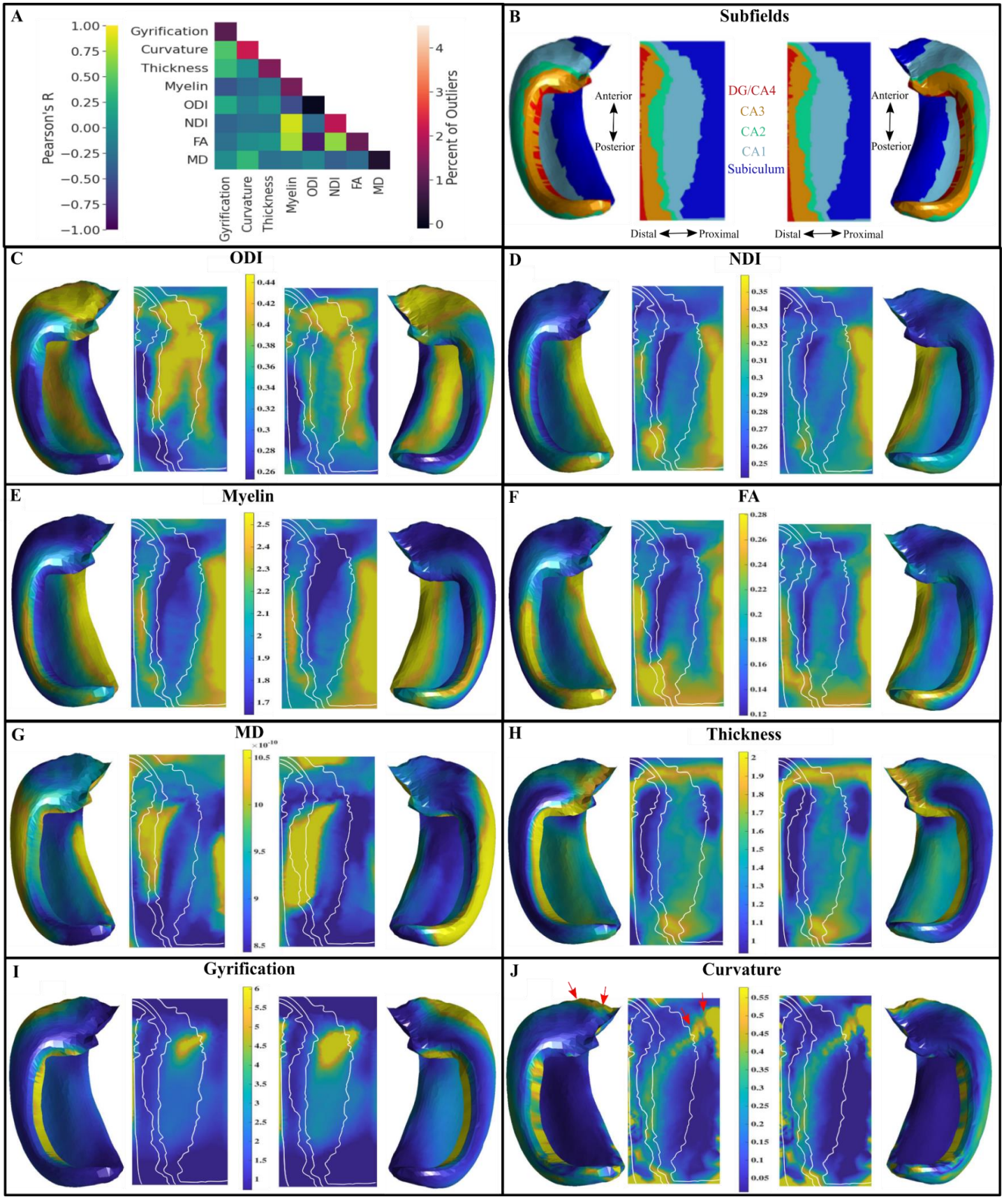

Figure 2. Correlations and plots of mean macro- and microstructure metrics on averaged hippocampal midthickness surfaces in folded and unfolded space for left and right hemispheres. (A) Heatmap showing Pearson's R correlations after correlating all average map vertices between two metrics, combining both left and right hemispheres. The on-diagonal elements represent the percent of outliers for each average map shown in (C-J). (B) Left and right hippocampal subfields from a manual segmentation of a histological reference (Ammunts et al., 2013; DeKraker et al., 2020). Unfolded space is shown in the same orientation for left and right hemispheres. DG - Dentate Gyrus, CA - Cornu Ammonis. (C,D) Orientation Dispersion Index (ODI) and Neurite Density Index (NDI) from NODDI. White lines represent subfield borders shown in (B). (E) Myelin content. (F,G) Diffusion Tensor Imaging metrics of Fractional Anisotropy (FA) and Mean Diffusivity (MD - m^2/s). (H-J) Macrostructure measures of thickness, gyrification, and curvature. (J) Red arrows highlight the highly curved "spine" of the hippocampus.

Inner-Outer alignment: High IO alignment seen in CA1 is likely a result of the pyramidal neurites. The pyramidal somas exist in the stratum pyramidale layer of the midthickness surface, and are generally scattered in CA1 (Nieuwenhuys et al., 2008). Their axons and basal dendrites move IO towards the alveus/outer surface and their large apical dendrites move IO towards the stratum radiatum/inner surface. All IO alignment seen in CA1 would be expected to be caused by the pyramidal neurites or other afferent CA1 paths such as the Schaffer collaterals which curve IO before making contact with the apical dendrites of the pyramidal neurites. High IO alignment in the subiculum is also likely caused by pyramidal neurites as in CA1.

The cosine similarities across subjects varied the greatest in CA1 and the subiculum across AP, PD, and IO directions (supplementary Figure 3).

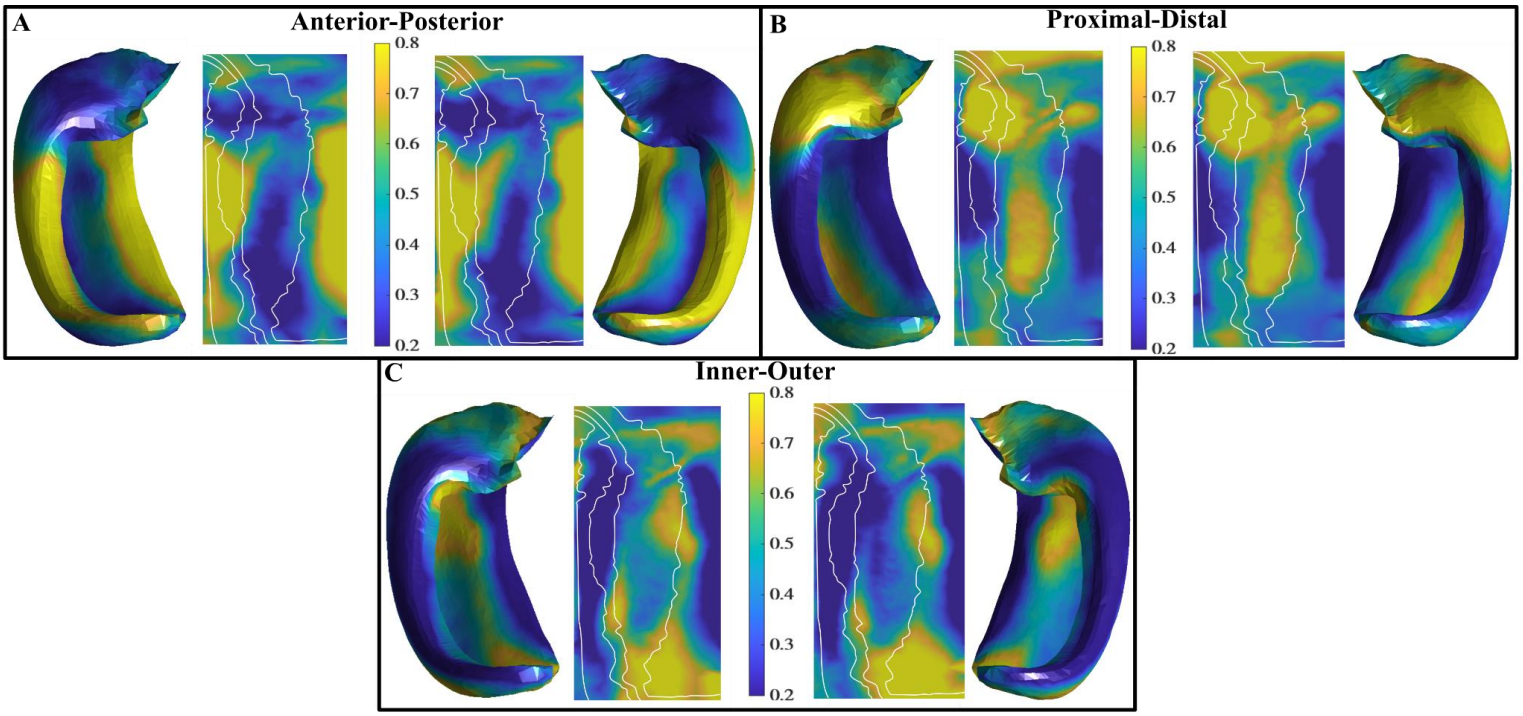

Figure 3. Mean of the cosine similarities between hippocampal axis vectors and NODDI vectors in the left and right hemisphere along the midthickness surface. High cosine similarities correspond to a high alignment of the NODDI vector along that particular hippocampal axis. (A) Distribution of cosine similarities along the anterior-posterior direction. (B) Distribution of cosine similarities along the proximal-distal (tangential) direction. (C) Distribution of cosine similarities along the inner-outer (laminar) direction.

3.6 Stability Analysis

The results of the stability analysis can be seen in Figure 4. Figure 4A presents the stability and the gradient in the reconstruction error using all the metrics combined that are shown in Figure 4B-E. The goal of the stability analysis was to elucidate the largest component value that was still stable and provided a relative gain in reconstruction error. In Figure 4A it can be seen that a component solution of k=6 has good stability with relatively low standard deviation. Comparatively, decomposing into a larger number of components decreases the stability of the OPNNMF solution. As well, k=6 does provide a relative gain in reconstruction error, although the largest gain in reconstruction error occurs when moving from a k=2 to a k=3 solution. The stability

analysis suggests that k=6 is the highest component value that is largely stable, thus we use this for the decomposition results using all metrics.

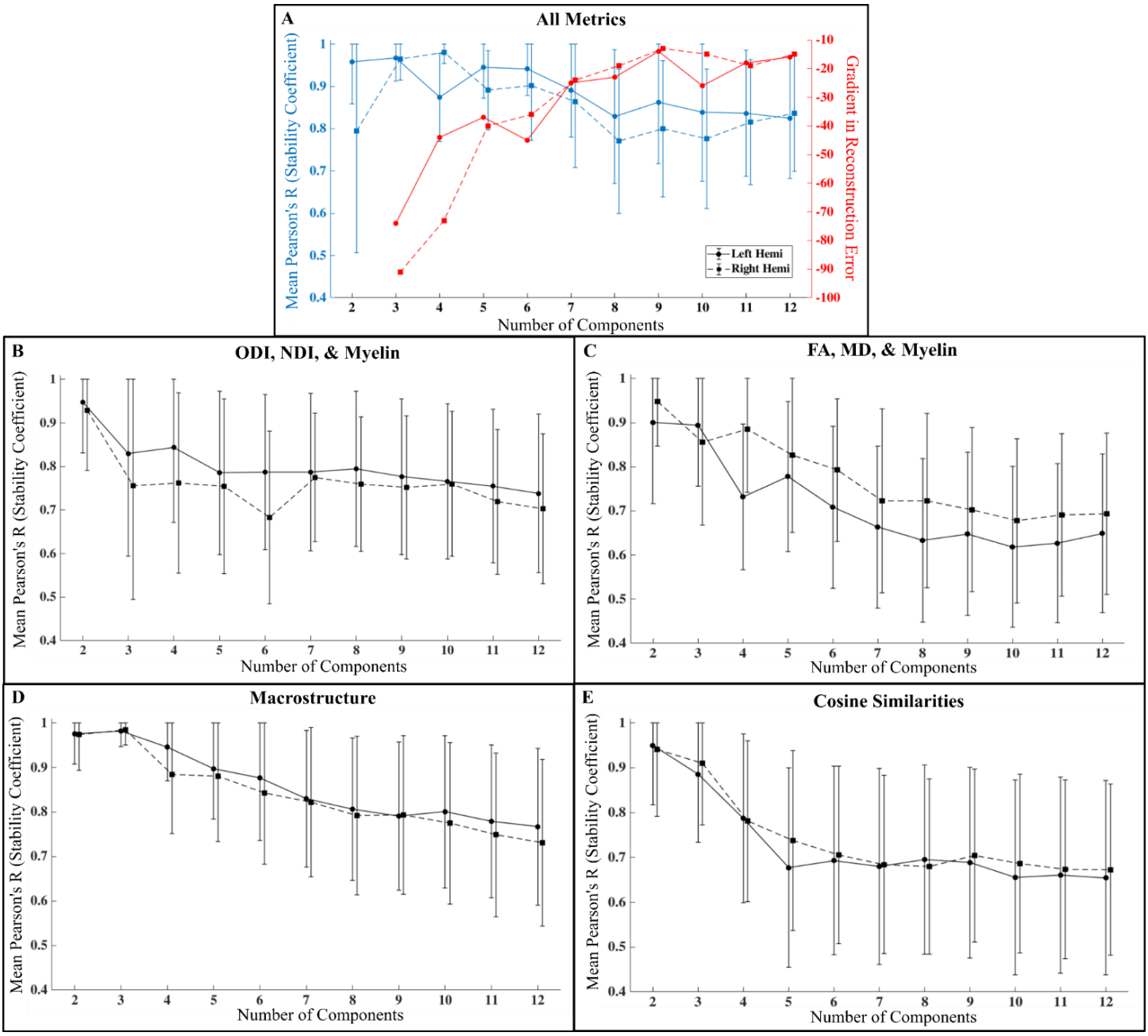

Figure 4. Stability coefficient and the gradient in reconstruction error based on the number of components used for the OPNNMF solution. Filled in circles plus solid lines are the left hemisphere and filled in squares plus dotted lines are the right hemisphere. Error lines show +- 1 SD. (A) Stability coefficient (blue) and the gradient in reconstruction error (red) as a function of the number of components using all metrics for NMF in B-E. (B) Stability coefficient for NODDI

metrics (ODI and NDI) plus myelin (T1w/T2w). (C) Stability coefficient for DTI metrics (FA and MD) plus myelin (T1w/T2w). (D) Stability coefficient for macrostructure metrics (gyrification, thickness, curvature). (E) Stability coefficient for cosine similarities (AP, PD, and IO). Points between hemispheres are slightly offset along the x-axis so that error bars are visible.

Another goal of the stability analysis was to compare the stability of the decomposition using all metrics versus using smaller groupings of metrics, such as NODDI (ODI and NDI) plus myelin. Comparing Figure 4A with Figure 4B-E, it can be seen that for almost all component values the all metric solution tends to be more stable than any of the smaller metric groupings. This is especially true for the larger component values above k=6. These results suggest that the use of multiple metrics results in more stable parcellations, as found in Patel et al. (2020).

The 6-component solution using all metrics is presented in Figure 5 for both the left and right hippocampus. 4-component solutions for all smaller metric combinations shown in Figure 4B-E can be found in supplementary Figure 6.

3.7 Description of the 6-component Solution

Figure 5A depicts the winner-take-all method applied at each vertex in folded and unfolded space for 6-components. Figure 5B shows the z-scored subject-metric weight matrices. In the following paragraph we describe the first 3 components including their location relative to the subfields (proximal-distal/medial-lateral axes) as well as along the anterior-posterior (longitudinal) axis. We also describe the features which contribute to each component. We then provide a general description of the 6-component solution as a whole rather than in parts. The left and right hippocampus do have similar covariance patterns although the component numbers differ. We will adopt the ordering of the left hippocampus for the rest of the paper, which we will take as reference to the spatially analogous region in the right hemisphere (ex. The spatial location of component 1 of the left hemisphere corresponds to the location of component 2 of the right hemisphere).

Component 1 is characterized by a cluster of vertices through the body and tail of the most proximal edge of the subiculum and through the body and tail of CA3. This component spans around the bottom two-thirds of the hippocampus across its anterior-posterior axis. Component 1 is characterized by high NDI, myelin, FA, and AP cosine similarity. This likely reflects the large AP oriented fiber bundles that are myelinated such as the cingulum bundle for the proximal edge subiculum and the fimbria for CA3.

Component 2 is characterized by vertices that are present only in the body or middle one-third along the anterior-posterior axis of CA1. This component is characterized by high ODI, gyrification, and PD and IO cosine similarities. This likely reflects a high heterogeneity in fiber orientation in CA1.

Component 3 is characterized by vertices that cross the subiculum and CA1 in a proximal-distal fashion in the head of the hippocampus, as well as vertices that span the anterior-posterior body of the hippocampus at the border between the subiculum and CA1. This component is characterized by high ODI, thickness, and IO cosine similarity.

A general pattern is noticed when examining the whole 6-components rather than looking at its parts. Generally, the middle one-third along the anterior-posterior axis (body) seems to have more parcellations than the top or bottom one-third (head and tail, respectively). That is, more parcellations exist along the proximal-distal direction in the body than do in the head or tail.

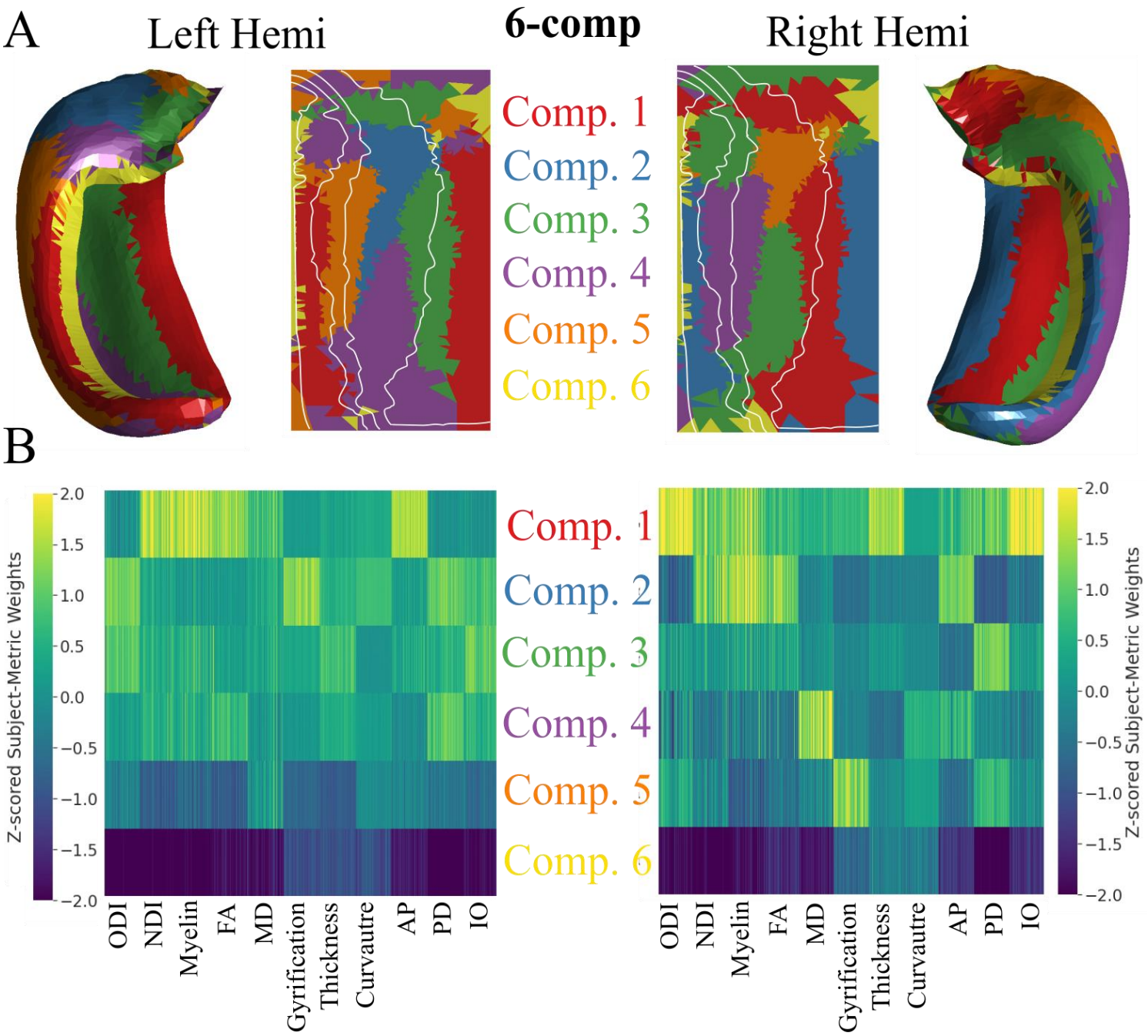

Figure 5. 6-component NMF solution on the midthickness surface for left and right hippocampi. (A) Winner-take all output at each vertex shown in folded and unfolded space. White lines denote subfield borders. (B) Z-scored subject-metric weight matrices across each of the 6 components, denoting the z-scored contribution of each metric to each component. AP, PD, and IO represent the 3 cosine similarity metrics.

4. Discussion

In the current study we examined the microstructure of the hippocampus across its subfields using the in vivo HCP dMRI data and NODDI, along with structural data to utilize novel surface-based methods. We found that ODI was highest in the CA1 and subiculum subfields, likely capturing the large heterogeneity of tangential and radial fibers. NDI and myelin were found to be strongly correlated and were highest in the subiculum and lowest in CA1, suggesting that NODDI may contain information about myelinated neurites. OPNNMF components appeared to capture unique co-varying clusters within the hippocampus, with high medial-lateral and long-axis variability. Finally, we found that by examining the main direction of diffusion relative to the three hippocampal axes, we could elucidate unique orientations which likely correspond to specific microstructural properties.

4.1 Dispersion of neurites in the hippocampus may reflect heterogeneous radial and tangential neurite components

The Orientation Dispersion Index (ODI) is meant to characterize the variation in neurite orientation around a single dominant direction at every voxel. A previous study using ODI and patch-wise circular variance measured using histology (measures variability in neurite orientations) has shown that both measures have lower dispersion in demyelinated lesions in patients with multiple sclerosis, where there is reduced geometrical complexity of neurites (Grussu et al., 2017). The hippocampal gray matter has a general distribution of microstructure that is similar to the neocortex, with tangential (proximal-distal) and radial (inner-outer) components that follow the curvature of the hippocampus. In the current study we showed that CA1 has the largest ODI, and thus can be considered to have the largest heterogeneity in neurite orientations. CA1 has large tangential neural processes, like the Schaffer collaterals and perforant path, as well as a large (yet dispersed) radial pyramidal neurite layer (Duvernoy et al., 2013). By measuring the orientation of the main direction of diffusion relative to the three hippocampal axes in CA1 (Figure 3), we found

either high tangential or radial diffusion, supporting the idea that ODI reflects the heterogeneity of these components. Conversely, ODI is lower in DG/CA4, CA3, and at the most proximal edge of the subiculum. In these regions the main diffusion direction was minimally tangential or radial, and was largely anterior-posterior or oblique. The apparent reduction in measured heterogeneity of tangential and radial components may potentially explain the low ODI in these regions. In the DG/CA4 and CA3 region this could be a result of partial voluming with the nearby fimbria, and in the subiculum it could be due to partial voluming with the nearby cingulum bundle or the perforant path at its most proximal edge. As hypothesized in the rest of the cortex (Fukutomi et al., 2018), it is likely that ODI in the hippocampal gray matter is largely driven by the heterogeneity of radial and tangential neurite components.

4.2 Hippocampal neurite density is highly correlated with measures of myelin

The distribution of the NDI and myelin across hippocampal gray matter was similar, as seen in Figure 2D and E and as shown by their strong positive correlation. While the diffusion signal is generally agnostic to water within myelin, previous work has shown that myelinated axons restrict diffusion to a greater degree than unmyelinated axons (Behrens & Johansen-Berg, 2014), suggesting that NDI may reflect the density of myelinated axons. The myelin content and NDI was largest in the body and tail of the subiculum. High myelin content in the subiculum has been noted previously with histology (Ding & Van Hoesen, 2015). Furthermore, it is likely that the white matter of the cingulum bundle or perforant path contribute to the large myelin content seen in the subiculum. Conversely, myelin and NDI were lower in CA1, which is likely a result of decreased density of pyramidal cells along the midthickness surface or the unmyelinated Schaffer collaterals (Jürgen et al., 2011; Szirmai et al., 2012). Overall, the distribution of myelin found here agrees with previous studies (DeKraker et al., 2018; Ábrahám et al., 2012). A strong positive correlation between NDI and myelin was found previously across the cortex. However, the hippocampus was found to have moderate values in NDI but low values of myelin when compared to the rest of the

cortical areas (Fukutomi et al., 2018). Here we show that a strong correlation between NDI and myelin still exists in the hippocampus when comparing them at a finer spatial scale. This correlation is further corroborated by another cortical study at high *ex-vivo* resolutions in the rodent brain, in which cortical NDI was strongly correlated with staining intensity of myelinated axons (Jespersen et al., 2010). Histological work has found similar correlations in white matter, where myelin content was found to be strongly correlated with axon count (Schmierer et al., 2007). However, a recent study utilizing a multicomponent relaxometry method for imaging myelin water fraction found no significant correlation between myelin and NDI measured using NODDI in most white matter structures (Qian et al., 2020). While NDI and myelin do appear to be correlated in gray matter including the hippocampus, further work is needed to examine this correlation in other white matter structures, including white matter surrounding the hippocampus such as the fimbria, fornix, and alveus.

4.3 Microstructure metrics follow subfield borders

Microstructural metrics such as intracortical myelin and macrostructural cortical thickness have been shown to be useful in parcellating the neocortex into subregions (Nieuwenhuys, 2013; Glasser et al., 2014; Glasser & Van Essen, 2011). Furthermore, using non-negative matrix factorization of intracortical myelin, MD, and FA it was found that a 4-component solution qualitatively resembled hippocampal subfield borders (Patel et al., 2020), suggesting that myelin and microstructure may provide sufficient separability to parcellate hippocampal subfields. In the current study, we qualitatively found that myelin, NDI, and ODI closely correspond to the subfield borders (Figure 2). Critically, it appears that NDI and ODI more closely correspond to the subfield borders then FA and MD, suggesting that NODDI may be more useful than DTI in capturing known microstructural differences across subfields. Furthermore, the usefulness of standard DTI in the hippocampus is likely limited since FA and MD are understated in regions of crossing fibers. Myelin has been demonstrated previously to closely correspond to averaged subfield borders

(DeKraker et al., 2018). To a lesser extent, macrostructure appears to also follow the subfield borders, which has been noted previously for thickness (DeKraker et al., 2018). While thickness is consistently low in CA3 and CA2, and gyrification is consistently high in CA1, these measures alone may not differentiate all subfield boundaries. Thus, a combination of NODDI and macrostructural measures may provide complimentary information needed for subject-specific subfield delineation. Future studies should quantify the utility of myelin and NODDI metrics to parcellate hippocampal subfields.

4.4 Strong correlations between NDI and MD along with ODI and FA

In the current study we found relatively strong correlations between NDI and MD and ODI and FA (Figure 2A). A previous post-mortem study in white matter found that MD was strongly negatively correlated with NDI (Schmierer et al., 2011). Furthermore, a correlation study in the whole cortex found a moderate correlation between NDI and MD when using the standard b = 1000 s/mm^2 shell for the DTI calculation (as done here), and a strong correlation between the two when using all shells (b = 1000, 2000, 3000 s/mm^2) to fit the DTI model (Fukutomi et al., 2018). They also found strong correlations between ODI and FA using both methods of DTI fitting. Recently, the same group has shown that DTI parameters with lower b-values suffer from non-negligible CSF contributions and significant partial voluming, while high b-value DTI parallels metrics calculated by NODDI in the cortex (Fukutomi et al., 2019). Thus, future work could use higher b-values to calculate DTI metrics where a stronger correlation with NODDI metrics would be expected in the hippocampus.

4.5 Orientation cosine similarities may be useful in identifying hippocampal microstructure

Typical hippocampal microstructural analyses average scalar diffusion metrics (such as FA, MD, NDI, etc.) either across whole hippocampi (van Uden et al., 2015; Salmenpera et al., 2006) or whole subfields (Radhakrishnan et al., 2020), which are inherently non-specific towards microstructure which exists within and across subfields. Here we quantified the main direction of

diffusion relative to the 3 main hippocampal axes which microstructure tends to align closely with. The orientational analyses described here have the potential to increase specificity at *in vivo* resolutions by utilizing known anatomical microstructure orientation. Future studies should use other methods of diffusion orientation representation, such as the Orientation Distribution Function (ODF) to capture crossing fibers. The peaks of the ODF can be used to quantify the relative amount of diffusion along the hippocampal axes which can be related to known microstructure orientations.

Applications of the proposed orientational methods may be useful to identify microstructure deterioration in disease states, where affected microstructure may be less prominent, and may appear as smaller cosine similarities along a particular axis. For example, perforant path lesions in rats caused rapid memory loss which was akin to early-stage Alzheimer's disease (Kirkby & Higgins, 2001). A 2010 study found deterioration of the perforant path in aged humans using diffusion tensor imaging (Yassa et al., 2010). Perforant path degradation should result in less attenuation of the diffusion signal along its length, which may potentially show up as smaller PD cosine similarities specifically in the subiculum, CA3, and CA1, as there should be less PD oriented diffusion. This may be possible for other neurological diseases where specific microstructure is affected, such as pyramidal neurite degradation which should result in smaller IO cosine similarities. However, to draw such conclusions, further *ex vivo* validation with tractography, which has been shown to be useful in capturing the microstructure described above, will be essential to evaluate the usefulness of this method (Beaujoin et al. 2018).

4.6 6-component OPNNMF solution displays the two main dimensions of hippocampal organization

The hippocampus is believed to have two main interacting dimensions of organization along its medial-lateral/proximal-distal or subfield axis, and across its long or anterior-posterior axis (see Genon et al., 2021 for review). In the current study with a 6-component OPNNMF solution we

found a varying number of parcellations along the medial-lateral direction, suggesting that regions along this axis have disparate macro- and microstructural properties. Variability along this axis is expected, as the subfields show differences in morphology, cytoarchitectonic profiles (Duvernoy et al., 2013; Ding & Van Hoesen, 2015), and connectivity (Andersen et al., 1971). Recently there has been interest in the long-axis organization of the hippocampus, with strong evidence coming from anatomical and physiological recordings in rodents (Chase etal., 2015). In the current study we found more proximal-distal (medial-lateral) parcels in the body than in the head and tail of the hippocampus. Previous research using task-based and resting-state functional connectivity found similar clusters, with more medial-lateral clusters in the body then in the head or tail (Plachti et al., 2019). While the head, body, and tail are often distinguished by task-based and resting state functional MRI (tripartite model, Genon et al., 2021), here we show that these segments along the anterior-posterior axis can also be identified when combining multiple disparate metrics into one decomposition.

4.7 Using a surface-based approach is ideal for characterizing the hippocampus

Accurately aligning and segmenting the hippocampus across individuals is important in order to provide anatomically meaningful results. However, inter-individual variability in the anterior-posterior curvature and number of digitations of the hippocampus makes alignment and parcellation into subfields a unique challenge (Ding & Van Hoesen, 2015; ten Hove & Poppenk, 2020; DeKraker et al., 2018). The issue of inter-individual variability of the hippocampus is typically solved in one of two ways. First, manual segmentations aim to identify landmarks that can be seen in histology and MRI that are consistently oriented to subfield boundaries across individuals (DeKraker et al., 2021b). However, the alignment of landmarks is highly dependent on the slice angle of the MRI and anterior-posterior distance along the hippocampus (head, body, tail) (DeKraker et al., 2021b). Many manual protocols will also only segment the less complex body of the hippocampus, opting to leave out the more complex head and tail. Second, reference

atlases can be computationally registered to fit a given subject (DeKraker et al., 2021b). This is most commonly used in automated segmentation methods. Automated methods are advantageous for their reproducibility, efficiency, and ability to account for curvature along the anterior-posterior axis. However, it is typically unclear how to register hippocampi with varying numbers of digitations. In such cases, one digitation could be stretched over multiple reference digitations, or vice versa (DeKraker et al., 2021b). This can cause major distortions in the resulting segmentations, losing the known contiguity of hippocampal subfields and creating issues when all subjects are aligned to a reference space. The current approach utilized *HippUnfold:* a novel surface-based tool to segment the hippocampal subfields and project hippocampi to a 2D unfolded space where they are aligned on the basis of topology and contiguity (DeKraker et al., 2018; DeKraker et al., 2021a). The surface-based approach used here can account for interindividual differences in tissue curvature and digitation across the whole anterior-posterior extent of the hippocampus (DeKraker et al., 2021b). Interpretations also become much simpler and apparent in unfolded space compared to results in 3D native space. Furthermore, at high resolutions a surface-based approach can allow for characterization of metrics across the laminar layers of the hippocampus. Finally, this approach can be used to capture the head and tail of the hippocampus, which other studies typically avoid due to its complexity.

4.8 NODDI optimization in hippocampal gray matter

NODDI has been validated by histology and *ex-vivo* MRI, where ODI and NDI appear to have high construct validity (Grussu et al., 2017). However, the original parameterization of the NODDI model assumes the intracellular and extracellular parallel diffusivity values are equal to $1.7 \times 10^{-3} \frac{mm^2}{s}$, which is sufficient for white matter but has been shown to not be accurate in gray matter. In gray matter, a parallel diffusivity value of $1.1 \times 10^{-3} \frac{mm^2}{s}$ has consistently been shown to achieve the lowest mean squared error when fitting NODDI (Guerrero et al., 2019; Fukutomi et

al., 2018), and as such we adopted this value for our modeling here. However, no study has examined whether this assumption holds true specifically in the hippocampus. It may not be unreasonable to assume that the 3-layered hippocampal allocortex may have different diffusivity values than the 6-layered neocortex. Thus, future studies should look to examine and optimize diffusivity values in the hippocampus to improve the accuracy of NODDI metrics. Another assumption of the NODDI model is the equality of the intracellular and extracellular parallel diffusivity. While this assumption is seen as more valid in gray matter than white matter (Jelescu et al., 2015, Jelescu et al., 2016), a recent study using a general framework to map microstructural metrics including diffusivity values found that while intraneurite diffusion in gray matter was around $1.1 \times 10^{-3} \frac{mm^2}{s}$, the extracellular parallel diffusivity was much higher (Novikov et al., 2018). The validity of NODDI assumptions and characterization of hippocampal diffusivity should be investigated further in the hippocampus.

5. Conclusion

In the current study we show distinct *in-vivo* microstructural distributions and orientations within and across the hippocampal subfields, something that has not been investigated with comparable granularity up to this point. Furthermore, we provide context for the use of surface-based approaches to investigate hippocampal microstructure.

Our findings have several important implications for future work. The hippocampus is particularly vulnerable to certain neurological diseases such as Alzheimer ’s disease and epilepsy, in which it is often one of the earliest aberrant structures (Dhikav et al., 2012). Examining the microstructure of the hippocampus at fine spatial resolutions in the simplified unfolded space, as done in this study, may provide potentially useful clinical imaging markers of hippocampal integrity. Furthermore, we noticed relatively large radial and tangential components of diffusion mainly in CA1 and the subiculum. Future work could attempt to tease apart these two orientationally distinct populations, providing estimates which may be useful to examine

microstructurally specific deterioration. Furthermore, using the same orientation methods in this study, future work should focus on capturing multiple microstructure orientations as the hippocampus contains many crossing fibers. Future work could also relate all the identified OPNNMF components to demographic and cognitive variables to identify if there is a relationship between variability in cognitive performance and variability in the metrics used in this study. Finally, the macro- and microstructural metrics observed in this study appear to show good separability between hippocampal subfields, suggesting they may be useful in future subfield parcellations.

Acknowledgements

This work was supported in part by funding provided by Brain Canada, in partnership with Health Canada, for the Canadian Open Neuroscience Platform initiative. BK is supported by a post-graduate scholarship from the Natural Sciences and Engineering Research Council of Canada (NSERC). JD is supported by a postdoctoral fellowship NSERC grant. ARK was supported by the Canada Research Chairs program (#950-231964), NSERC Discovery Grant (#6639), and Canada Foundation for Innovation (CFI) John R. Evans Leaders Fund project (#37427), the Canada First Research Excellence Fund, and Brain Canada. ARK and SK were supported by a Canadian Institute for Health Research grant (CIHR Project grant #366062). SK is supported by a NSERC discovery grant (#05770). This research was enabled in part by the support provided by the Digital Research Alliance of Canada. Data collection and sharing for this project was provided by the Human Connectome Project (HCP; Principal Investigators: Bruce Rosen, M.D., Ph.D., Arthur W. Toga, Ph.D., Van J. Weeden, MD). HCP funding was provided by the National Institute of Dental and Craniofacial Research (NIDCR), the National Institute of Mental Health (NIMH), and the National Institute of Neurological Disorders and Stroke (NINDS). HCP data are disseminated by the Laboratory of Neuro Imaging at the University of Southern California.

References

Ábrahám, H., Vincze, A., Veszprémi, B., Kravják, A., Gömöri, É., Kovács, G. G., & Seress, L. (2012). Impaired myelination of the human hippocampal formation in down syndrome. *International Journal of Developmental Neuroscience*, *30*(2), 147–158. https://doi.org/10.1016/j.ijdevneu.2011.11.005

Amunts, K., Lepage, C., Borgeat, L., Mohlberg, H., Dickscheid, T., Rousseau, M.-E., Bludau, S., Bazin, P.-L., Lewis, L. B., Oros-Peusquens, A.-M., Shah, N. J., Lippert, T., Zilles, K., & Evans, A. C. (2013). Bigbrain: An ultrahigh-resolution 3d human brain model. *Science*, *340*(6139), 1472–1475. https://doi.org/10.1126/science.1235381

Andersen, P., Bliss, T. V. P., & Skrede, K. K. (1971). Lamellar organization of hippocampal excitatory pathways. *Experimental Brain Research*, *13*(2). https://doi.org/10.1007/bf00234087

Andersson, J. L. R., & Sotiropoulos, S. N. (2015). Non-parametric representation and prediction of single- and multi-shell diffusion-weighted MRI data using Gaussian processes. *NeuroImage*, *122*, 166–176. https://doi.org/10.1016/j.neuroimage.2015.07.067

Assaf, Y., & Basser, P. J. (2005). Composite hindered and restricted model of diffusion (charmed) MR imaging of the human brain. *NeuroImage*, *27*(1), 48–58. 10.1016/j.neuroimage.2005.03.042

Assaf, Y., Blumenfeld-Katzir, T., Yovel, Y., & Basser, P. J. (2008). Axcaliber: A method for measuring Axon diameter distribution from diffusion MRI. *Magnetic Resonance in Medicine*, *59*(6), 1347–1354. 10.1002/mrm.21577

Assaf, Y., & Cohen, Y. (2000). Assignment of the water slow-diffusing component in the central nervous system using Q-Space Diffusion Mrs: Implications for Fiber Tract Imaging. *Magnetic Resonance in Medicine*, *43*(2), 191–199. https://doi.org/10.1002/(sici)1522-2594(200002)43:2<191::aid-mrm5>3.0.co;2-b

Basser, P. J., Mattiello, J., & LeBihan, D. (1994). Mr diffusion tensor spectroscopy and imaging. *Biophysical Journal*, *66*(1), 259–267. https://doi.org/10.1016/s0006-3495(94)80775-1

Beaujoin, J., Palomero-Gallagher, N., Boumezbeur, F., Axer, M., Bernard, J., Poupon, F., . . . Poupon, C. (2018). Post-mortem inference of the human Hippocampal connectivity and microstructure using ultra-high field diffusion MRI at 11.7 T. *Brain Structure and Function*, *223*(5), 2157-2179.

Behrens, T., & Johansen-Berg, H. (2014). *Diffusion Mri: From quantitative measurement to in vivo neuroanatomy*. Elsevier.

Bendel, O., Bueters, T., Euler, M. V., Ögren, S. O., Sandin, J., & Euler, G. V. (2005). Reappearance of Hippocampal CA1 Neurons after Ischemia is Associated with Recovery of Learning and Memory. *Journal of Cerebral Blood Flow & Metabolism*, *25*(12), 1586-1595. 10.1038/sj.jcbfm.9600153

Blümcke, I., Coras, R., Miyata, H., & Özkara, C. (2012). Defining clinico-neuropathological subtypes of Mesial Temporal Lobe Epilepsy with hippocampal sclerosis. *Brain Pathology*, *22*(3), 402–411. https://doi.org/10.1111/j.1750-3639.2012.00583.x

Boutsidis, C., & Gallopoulos, E. (2008). SVD based initialization: A head start for nonnegative matrix factorization. *Pattern Recognition*, *41*(4), 1350–1362. https://doi.org/10.1016/j.patcog.2007.09.010

Burggren, A. C., Zeineh, M. M., Ekstrom, A. D., Braskie, M. N., Thompson, P. M., Small, G. W., & Bookheimer, S. Y. (2008). Reduced cortical thickness in hippocampal subregions among cognitively normal apolipoprotein e E4 carriers. *NeuroImage*, *41*(4), 1177–1183. https://doi.org/10.1016/j.neuroimage.2008.03.039

Campbell, J. S. W., Siddiqi, K., Rymar, V. V., Sadikot, A. F., & Pike, G. B. (2005). Flow-based fiber tracking with diffusion tensor and Q-ball data: Validation and comparison to principal diffusion direction techniques. *NeuroImage*, *27*(4), 725–736. https://doi.org/10.1016/j.neuroimage.2005.05.014

Chase, H. W., Clos, M., Dibble, S., Fox, P., Grace, A. A., Phillips, M. L., & Eickhoff, S. B. (2015). Evidence for an anterior–posterior differentiation in the human hippocampal formation revealed by meta-analytic parcellation of fmri coordinate maps: Focus on the Subiculum. *NeuroImage*, *113*, 44–60. https://doi.org/10.1016/j.neuroimage.2015.02.069

Cheng, H., Zhu, H., Zheng, Q., Liu, J., & He, G. (2020). Functional parcellation of the hippocampus by semi-supervised clustering of resting state fmri data. *Scientific Reports*, *10*(1). https://doi.org/10.1038/s41598-020-73328-1

Cherubini, E., & Miles, R. (2015). The CA3 region of the hippocampus: How is it? What is it for? How does it do it? *Frontiers in Cellular Neuroscience*, *9*. 10.3389/fncel.2015.00019

Coras, R., Milesi, G., Zucca, I., Mastropietro, A., Scotti, A., Figini, M., Mühlebner, A., Hess, A., Graf, W., Tringali, G., Blümcke, I., Villani, F., Didato, G., Frassoni, C., Spreafico, R., & Garbelli, R. (2014). 7T MRI features in control Human hippocampus and hippocampal sclerosis: An ex vivo study with histologic correlations. *Epilepsia*, *55*(12), 2003–2016. https://doi.org/10.1111/epi.12828

DeKraker, J., Ferko, K., Lau, J., Köhler, S., & Khan, A. (2018). Unfolding the hippocampus: An intrinsic coordinate system for subfield segmentations and quantitative mapping. *NeuroImage*, *167*, 408418. 10.1016/j.neuroimage.2017.11.054

DeKraker, J., Haast, R. A. M., Yousif, M. D., Karat, B. G., Köhler, S., & Khan, A. R. (2021a). Hippunfold: Automated hippocampal unfolding, morphometry, and subfield segmentation. *bioRxiv*. https://doi.org/10.1101/2021.12.03.471134

DeKraker, J., Köhler, S., & Khan, A. R. (2021b). Surface-based hippocampal subfield segmentation. *Trends in Neurosciences*. https://doi.org/10.1016/j.tins.2021.06.005

DeKraker, J., Lau, J. C., Ferko, K. M., Khan, A. R., & Köhler, S. (2020). Hippocampal subfields revealed through unfolding and unsupervised clustering of laminar and morphological features in 3D BigBrain. *NeuroImage*, *206*, 116328. https://doi.org/10.1016/j.neuroimage.2019.116328

Dhikav, V., & Anand, K. S. (2012). Hippocampus in health and disease: An overview. *Annals of Indian Academy of Neurology*, *15*(4), 239. https://doi.org/10.4103/0972-2327.104323

Ding, SL., & Van Hoesen, G. W. (2015). Organization and detailed parcellation of human hippocampal head and body regions based on a combined analysis of cyto- and chemoarchitecture. *Journal of Comparative Neurology*, *523*(15), 2233–2253. https://doi.org/10.1002/cne.23786

Dinkelacker, V., Valabregue, R., Thivard, L., Lehéricy, S., Baulac, M., Samson, S., & Dupont, S. (2015). Hippocampal-thalamic wiring in medial temporal lobe epilepsy: Enhanced connectivity per hippocampal voxel. *Epilepsia*, *56*(8), 1217–1226. https://doi.org/10.1111/epi.13051

Duvernoy, H. M., Cattin, F., & Risold, P.-Y. (2013). *The human hippocampus functional anatomy, vascularization and serial sections with MRI*. Springer.

Fukutomi, H., Glasser, M. F., Murata, K., Akasaka, T., Fujimoto, K., Yamamoto, T., Autio, J. A., Okada, T., Togashi, K., Zhang, H., Van Essen, D. C., & Hayashi, T. (2019). Diffusion tensor model links to neurite orientation dispersion and density imaging at high B-value in cerebral cortical gray matter. Scientific Reports, 9(1). https://doi.org/10.1038/s41598-019-48671-7

Fukutomi, H., Glasser, M. F., Zhang, H., Autio, J. A., Coalson, T. S., Okada, T., Togashi, K., Van Essen, D. C., & Hayashi, T. (2018). Neurite imaging reveals

microstructural variations in human cerebral cortical gray matter. *NeuroImage*, *182*, 488–499.10.1016/j.neuroimage.2018.02.017

Garcia, K. E., Kroenke, C. D., & Bayly, P. V. (2018). Mechanics of cortical folding: Stress, growth and stability. *Philosophical Transactions of the Royal Society B: Biological Sciences*, *373*(1759), 20170321. https://doi.org/10.1098/rstb.2017.0321

Garyfallidis, E., Brett, M., Amirbekian, B., Rokem, A., van der Walt, S., Descoteaux, M., & Nimmo-Smith, I. (2014). Dipy, a library for the analysis of diffusion MRI data. *Frontiers in Neuroinformatics*, *8*. https://doi.org/10.3389/fninf.2014.00008

Genon, S., Bernhardt, B. C., La Joie, R., Amunts, K., & Eickhoff, S. B. (2021). The many dimensions of human hippocampal organization and (dys)function. *Trends in Neurosciences*, *44*(12), 977–989. https://doi.org/10.1016/j.tins.2021.10.003

Glasser, M. F., & Van Essen, D. C. (2011). Mapping human cortical areas in vivo based on myelin content as revealed by T1- and T2-weighted MRI. *Journal of Neuroscience*, *31*(32), 11597–11616. https://doi.org/10.1523/jneurosci.2180-11.2011

Glasser, M. F., Sotiropoulos, S. N., Wilson, J. A., Coalson, T. S., Fischl, B., Andersson, J. L., Xu, J., Jbabdi, S., Webster, M., Polimeni, J. R., Van Essen, D. C., & Jenkinson, M. (2013). The minimal preprocessing pipelines for the Human Connectome Project. *NeuroImage*, *80*, 105–124. https://doi.org/10.1016/j.neuroimage.2013.04.127

Glasser, M. F., Goyal, M. S., Preuss, T. M., Raichle, M. E., & Van Essen, D. C. (2014). Trends and properties of human cerebral cortex: Correlations with cortical myelin content. *NeuroImage*, *93*, 165–175. https://doi.org/10.1016/j.neuroimage.2013.03.060

Goodroe, S. C., Starnes, J., & Brown, T. I. (2018). The Complex Nature of Hippocampal-Striatal Interactions in Spatial Navigation. *Frontiers in Human Neuroscience*, *12*. 10.3389/fnhum.2018.00250

Grussu, F., Schneider, T., Tur, C., Yates, R. L., Tachrount, M., Ianuş, A., Yiannakas, M. C., Newcombe, J., Zhang, H., Alexander, D. C., DeLuca, G. C., & Gandini Wheeler-Kingshott, C. A. (2017). Neurite dispersion: A new marker of multiple sclerosis spinal cord pathology? *Annals of Clinical and Translational Neurology*, *4*(9), 663–679. https://doi.org/10.1002/acn3.445

Guerrero, J. M., Adluru, N., Bendlin, B. B., Goldsmith, H. H., Schaefer, S. M., Davidson, R. J., Kecskemeti, S. R., Zhang, H., & Alexander, A. L. (2019). Optimizing the fitting initial condition for the parallel intrinsic diffusivity in NODDI: An extensive empirical evaluation. https://doi.org/10.1101/630541

Halko, N., Martinsson, P. G., & Tropp, J. A. (2011). Finding structure with randomness: Probabilistic algorithms for constructing approximate matrix decompositions. *SIAM Review*, *53*(2), 217–288. https://doi.org/10.1137/090771806

Harms, R. L., Fritz, F. J., Tobisch, A., Goebel, R., & Roebroeck, A. (2017). Robust and fast nonlinear optimization of diffusion mri microstructure models. *NeuroImage*, *155*, 82–96. https://doi.org/10.1016/j.neuroimage.2017.04.064

Horner, A. J., Bisby, J. A., Bush, D., Lin, W., & Burgess, N. (2015). Evidence for holistic episodic recollection via hippocampal pattern completion. *Nature Communications, 6*(1). 10.1038/ncomms8462

Isensee, F., Jaeger, P. F., Kohl, S. A., Petersen, J., & Maier-Hein, K. H. (2020). NNU-net: A self-configuring method for deep learning-based biomedical image segmentation. *Nature Methods*, *18*(2), 203–211. https://doi.org/10.1038/s41592-020-01008-z

Jelescu, I. O., Veraart, J., Adisetiyo, V., Milla, S. S., Novikov, D. S., & Fieremans, E. (2015). One diffusion acquisition and different white matter models: How does microstructure change in human early development based on WMTI and Noddi? *NeuroImage*, *107*, 242–256. https://doi.org/10.1016/j.neuroimage.2014.12.009

Jelescu, I. O., Veraart, J., Fieremans, E., & Novikov, D. S. (2016). Degeneracy in model parameter estimation for multi-compartmental diffusion in neuronal tissue. *NMR in Biomedicine*, *29*(1), 33–47. https://doi.org/10.1002/nbm.3450

Jenkinson, M., Bannister, P., Brady, M., & Smith, S. (2002). Improved optimization for the robust and accurate linear registration and motion correction of brain images. *NeuroImage*, *17*(2), 825–841. https://doi.org/10.1006/nimg.2002.1132

Jespersen, S. N., Bjarkam, C. R., Nyengaard, J. R., Chakravarty, M. M., Hansen, B., Vosegaard, T., Østergaard, L., Yablonskiy, D., Nielsen, N. C., & Vestergaard-Poulsen, P. (2010). Neurite density from magnetic resonance diffusion measurements at ultrahigh field: Comparison with light microscopy and electron microscopy. *NeuroImage*, *49*(1), 205–216. https://doi.org/10.1016/j.neuroimage.2009.08.053

Jürgen M. K., Paxinos, G., Insausti, R., & Amaral, D. G. (2011). Hippocampal Formation. In *The Human Nervous System* (3rd ed., pp. 871–914). Elsevier Academic Press.

Kirkby, D. L., & Higgins, G. A. (2001). Characterization of perforant path lesions in rodent models of memory and attention. *European Journal of Neuroscience*, *10*(3), 823–838. https://doi.org/10.1046/j.1460-9568.1998.00087.x

Knierim, J. J. (2015). The hippocampus. *Current Biology*, *25*(3), R1116-R1121.

La Joie, R., Perrotin, A., de La Sayette, V., Egret, S., Doeuvre, L., Belliard, S., Eustache, F., Desgranges, B., & Chételat, G. (2013). Hippocampal subfield volumetry in mild cognitive impairment, Alzheimer's disease and semantic dementia. *NeuroImage: Clinical*, *3*, 155–162. https://doi.org/10.1016/j.nicl.2013.08.007

Liu, C., Ye, F. Q., Newman, J. D., Szczupak, D., Tian, X., Yen, C. C.-C., Majka, P., Glen, D., Rosa, M. G., Leopold, D. A., & Silva, A. C. (2020). A resource for the detailed 3D mapping of white matter pathways in the marmoset brain. *Nature Neuroscience*, *23*(2), 271–280. https://doi.org/10.1038/s41593-019-0575-0

Maillot, J., Yahia, H., & Verroust, A. (1993). Interactive texture mapping. *Proceedings of the 20th Annual Conference on Computer Graphics and Interactive Techniques - SIGGRAPH '93*. https://doi.org/10.1145/166117.166120

Moodley, K. K., & Chan, D. (2014). The hippocampus in neurodegenerative disease. *Frontiers of Neurology and Neuroscience*, 95–108. https://doi.org/10.1159/000356430

Nieuwenhuys, R., Huijzen, C. van, & Voogd, J. (2008). *The human central nervous system*. Springer.

Nieuwenhuys, R. (2013). The myeloarchitectonic studies on the human cerebral cortex of the Vogt-vogt school, and their significance for the interpretation of functional neuroimaging data. *Microstructural Parcellation of the Human Cerebral Cortex*, 55–125. https://doi.org/10.1007/978-3-662-45766-5_3

Novikov, D. S., Veraart, J., Jelescu, I. O., & Fieremans, E. (2018). Rotationally-invariant mapping of scalar and orientational metrics of neuronal microstructure with diffusion MRI. *NeuroImage*, *174*, 518–538. https://doi.org/10.1016/j.neuroimage.2018.03.006

Ozarslan, E., Koay, C.G., Shepherd, T., Blackband, S., & Basser, P. (2009). Simple harmonic oscillator based reconstruction and estimation for three-dimensional q-space MRI. *Proceedings of the International Society for Magnetic Resonance in Medicine*, 16.

Patel, R., Steele, C. J., Chen, A. G. X., Patel, S., Devenyi, G. A., Germann, J., Tardif, C. L., & Chakravarty, M. M. (2020). Investigating microstructural variation in the human hippocampus using non-negative matrix factorization. *NeuroImage*, *207*, 116348. https://doi.org/10.1016/j.neuroimage.2019.116348

Pedregosa, F., Varoquaux, G., Gramfort, A., Michel, V., Thirion, B., Grisel, O., Blondel, M., Prettenhofer, P., Weiss, R., Dubourg, V., Vanderplas, J., Passos, A., Cournapeau, D., Brucher, M., Perrot, M., & Duchesnay, É. (2011). Scikit-learn: Machine Learning in Python. *Journal of Machine Learning Research*, *12*(85), 2825–2830.

Pierpaoli, C., Jezzard, P., Basser, P. J., Barnett, A., & Di Chiro, G. (1996). Diffusion tensor MR imaging of the human brain. *Radiology*, *201*(3), 637–648. https://doi.org/10.1148/radiology.201.3.8939209

Plachti, A., Eickhoff, S. B., Hoffstaedter, F., Patil, K. R., Laird, A. R., Fox, P. T., Amunts, K., & Genon, S. (2019). Multimodal parcellations and extensive behavioral profiling tackling the hippocampus gradient. *Cerebral Cortex*, *29*(11), 4595–4612. https://doi.org/10.1093/cercor/bhy336

Plachti, A., Kharabian, S., Eickhoff, S. B., Maleki Balajoo, S., Hoffstaedter, F., Varikuti, D. P., Jockwitz, C., Caspers, S., Amunts, K., & Genon, S. (2020). Hippocampus co-atrophy pattern in dementia deviates from covariance patterns across the lifespan. *Brain*, *143*(9), 2788–2802. https://doi.org/10.1093/brain/awaa222

Poppenk, J., Evensmoen, H. R., Moscovitch, M., & Nadel, L. (2013). Long-axis specialization of the human hippocampus. *Trends in Cognitive Sciences*, *17*(5), 230–240. https://doi.org/10.1016/j.tics.2013.03.005

Qian, W., Khattar, N., Cortina, L. E., Spencer, R. G., & Bouhrara, M. (2020). Nonlinear associations of neurite density and myelin content with age revealed using multicomponent diffusion and relaxometry magnetic resonance imaging. *NeuroImage*, *223*, 117369. https://doi.org/10.1016/j.neuroimage.2020.117369

Quezada, S., van de Looij, Y., Hale, N., Rana, S., Sizonenko, S. V., Gilchrist, C., Castillo-Melendez, M., Tolcos, M., & Walker, D. W. (2020). Genetic and microstructural differences in the cortical plate of gyri and sulci during gyrification in fetal sheep. *Cerebral Cortex*, *30*(12), 6169–6190. https://doi.org/10.1093/cercor/bhaa171

Radhakrishnan, H., Stark, S. M., & Stark, C. E. (2020). Microstructural alterations in Hippocampal Subfields Mediate Age-related Memory decline in humans. *Frontiers in Aging Neuroscience*, *12*. https://doi.org/10.3389/fnagi.2020.00094

Raffelt, D. A., Tournier, J.-D., Smith, R. E., Vaughan, D. N., Jackson, G., Ridgway, G. R., & Connelly, A. (2017). Investigating white matter fibre density and morphology using fixel-based analysis. *NeuroImage*, *144*, 58–73. https://doi.org/10.1016/j.neuroimage.2016.09.029

Robinson, J. L., Barron, D. S., Kirby, L. A., Bottenhorn, K. L., Hill, A. C., Murphy, J. E., Katz, J. S., Salibi, N., Eickhoff, S. B., & Fox, P. T. (2015). Neurofunctional topography of the human hippocampus. *Human Brain Mapping*, *36*(12), 5018–5037. https://doi.org/10.1002/hbm.22987

Salmenpera, T. M., Simister, R. J., Bartlett, P., Symms, M. R., Boulby, P. A., Free, S. L., Barker, G. J., & Duncan, J. S. (2006). High-resolution diffusion tensor imaging of the hippocampus in temporal lobe epilepsy. *Epilepsy Research*, *71*(2-3), 102–106. https://doi.org/10.1016/j.eplepsyres.2006.05.020

Schmierer, K., Wheeler-Kingshott, C. A. M., Boulby, P. A., Scaravilli, F., Altmann, D. R., Barker, G. J., Tofts, P. S., & Miller, D. H. (2007). Diffusion tensor imaging of Post Mortem Multiple Sclerosis Brain. *NeuroImage*, *35*(2), 467–477. https://doi.org/10.1016/j.neuroimage.2006.12.010

Small, S. A., Schobel, S. A., Buxton, R. B., Witter, M. P., & Barnes, C. A. (2011). A pathophysiological framework of hippocampal dysfunction in ageing and disease. *Nature Reviews Neuroscience*, *12*(10), 585–601. https://doi.org/10.1038/nrn3085

Sotiras, A., Resnick, S. M., & Davatzikos, C. (2015). Finding imaging patterns of structural covariance via non-negative matrix factorization. *NeuroImage*, *108*, 1–16. https://doi.org/10.1016/j.neuroimage.2014.11.045

Sotiropoulos, S. N., Moeller, S., Jbabdi, S., Xu, J., Andersson, J. L., Auerbach, E. J., Yacoub, E., Feinberg, D., Setsompop, K., Wald, L. L., Behrens, T. E., Ugurbil, K., & Lenglet, C.

(2013). Effects of image reconstruction on fiber orientation mapping from multichannel diffusion mri: Reducing the noise floor using sense. *Magnetic Resonance in Medicine*, *70*(6), 1682–1689. https://doi.org/10.1002/mrm.24623

Strang, B. A., Witter, M. P., Lein, E. S., & Moser, E. I. (2014). Functional organization of the Hippocampal Longitudinal Axis. *Nature Reviews Neuroscience*, *15*(10), 655–669. https://doi.org/10.1038/nrn3785

Swanson, L. W., Wyss, J. M., & Cowan, W. M. (1978). An autoradiographic study of the organization of intrahippocampal association pathways in the rat. *The Journal of Comparative Neurology*, *181*(4), 681–715. https://doi.org/10.1002/cne.901810402

Szirmai, I., Buzsáki, G., & Kamondi, A. (2012). 120 years of hippocampal Schaffer Collaterals. *Hippocampus*, *22*(7), 1508–1516. https://doi.org/10.1002/hipo.22001

ten Hove, J., & Poppenk, J. (2020). Structural variation in hippocampal dentations among healthy young adults. https://doi.org/10.1101/2020.02.09.940726

Van Essen, D., Smith, S., Barch, D., Behrens, T., Yacoub, E., & Ugurbil, K. (2013). The WU-Minn Human Connectome Project: An overview. *NeuroImage*, *80*(62), 62-79.

van Uden, I. W. M., Tuladhar, A. M., van der Holst, H. M., van Leijsen, E. M. C., van Norden, A. G. W., de Laat, K. F., Rutten-Jacobs, L. C. A., Norris, D. G., Claassen, J. A. H. R., van Dijk, E. J., Kessels, R. P. C., & de Leeuw, F.-E. (2015). Diffusion tensor imaging of the HIPPOCAMPUS predicts the risk of dementia; the RUN DMC study. *Human Brain Mapping*, *37*(1), 327–337. https://doi.org/10.1002/hbm.23029

Voss, J. L., Bridge, D. J., Cohen, N. J., & Walker, J. A. (2017). A Closer Look at the Hippocampus and Memory. *Trends in Cognitive Sciences*, *21*(8), 577-588. 10.1016/j.tics.2017.05.008

Yang, & Oja, E. (2010). Linear and nonlinear projective nonnegative matrix factorization. *IEEE Transactions on Neural Networks*, *21*(5), 734–749.

https://doi.org/10.1109/tnn.2010.2041361

Yassa, M. A., Muftuler, L. T., & Stark, C. E. (2010). IC-P-056: Microstructural diffusion tensor Imaging reveals perforant path degradation in aged humans in vivo. *Alzheimer's & Dementia, 6*.

Yushkevich, P. A., Wang, H., Pluta, J., Das, S. R., Craige, C., Avants, B. B., Weiner, M. W., & Mueller, S. (2011). Nearly automatic segmentation of hippocampal subfields in in vivo focal T2-weighted MRI. *NeuroImage*, *53*(4), 1208–1224. https://doi.org/10.1016/j.neuroimage.2010.06.040

Zeineh, M. M., Holdsworth, S., Skare, S., Atlas, S. W., & Bammer, R. (2012). Ultra-high resolution diffusion tensor imaging of the microscopic pathways of the medial temporal lobe. *NeuroImage, 62*(3), 2065-2082.

Zhang, H., Schneider, T., Wheeler-Kingshott, C. A., & Alexander, D. C. (2012). NODDI: Practical in vivo neurite orientation dispersion and density imaging of the human brain. *NeuroImage*, *61*(4), 1000-1016. 10.1016/j.neuroimage.2012.03.072

Zhong, Q., Xu, H., Qin, J., Zeng, L.-L., Hu, D., & Shen, H. (2019). Functional parcellation of the hippocampus from resting-state dynamic functional connectivity. *Brain Research, 1715*, 165–175. https://doi.org/10.1016/j.brainres.2019.03.023

Zhou, Y., Dougherty, J. H., Hubner, K. F., Bai, B., Cannon, R. L., & Hutson, R. K. (2008). Abnormal connectivity in the posterior cingulate and hippocampus in early alzheimer's disease and mild cognitive impairment. *Alzheimer's & Dementia*, *4*(4), 265–270. https://doi.org/10.1016/j.jalz.2008.04.006

Supplementary Material

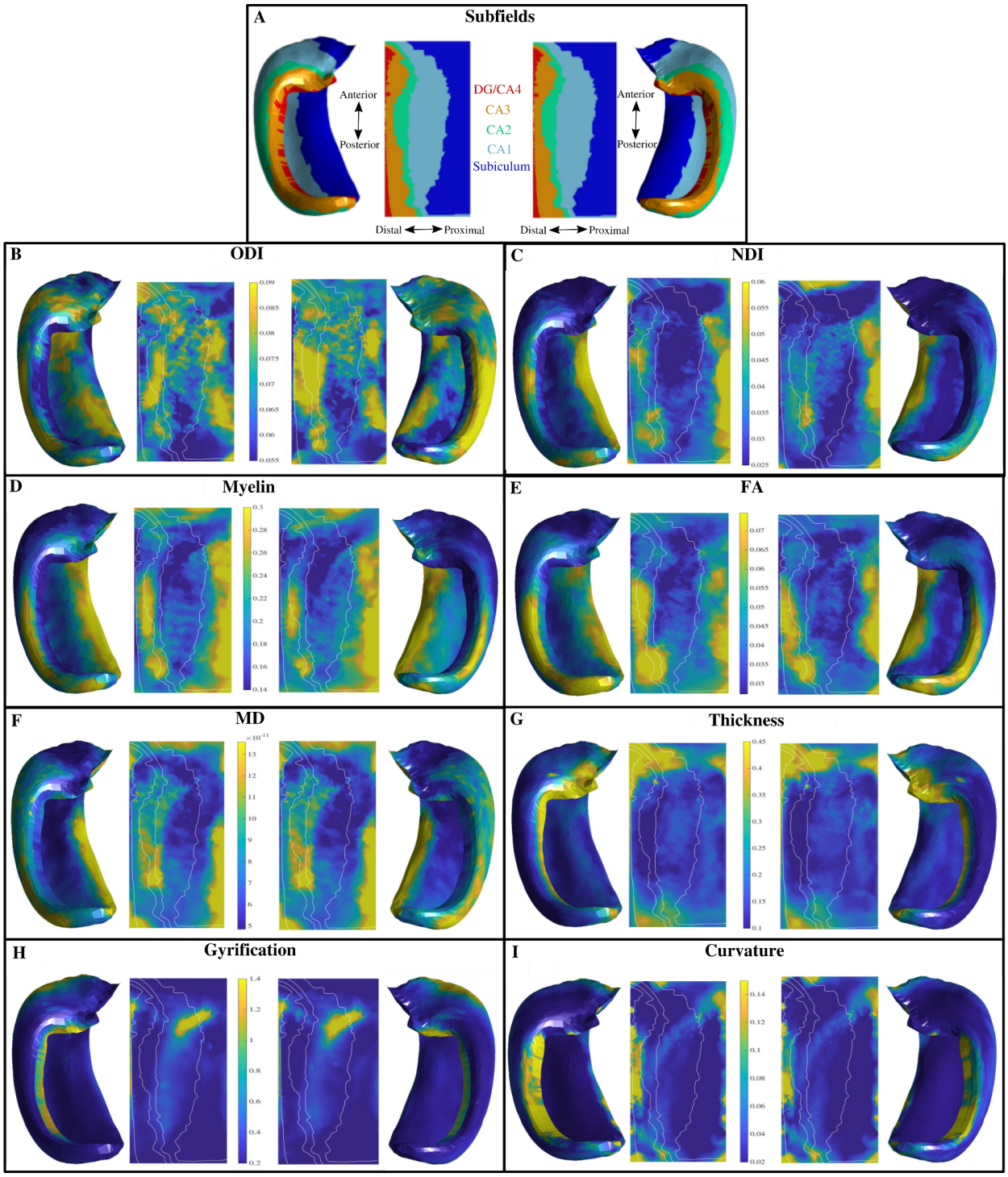

Supplementary Figure 1. Plots of the standard deviations for macro- and microstructure metrics on averaged hippocampal midthickness surfaces in folded and unfolded space for left and right hemispheres. (A) Left and right hippocampal subfields from a manual segmentation of a histological reference (Ammunts et al., 2013; DeKraker et al., 2020). Unfolded space is shown in the same orientation for left and right hemispheres. DG - Dentate Gyrus, CA - Cornu Ammonis.

(B,C) Orientation Dispersion Index (ODI) and Neurite Density Index (NDI) from NODDI. White lines represent subfield borders shown in (A). (D) Myelin content. (E,F) Diffusion Tensor Imaging metrics of Fractional Anisotropy (FA) and Mean Diffusivity (MD). (G-I) Macrostructure measures of thickness, gyrification, and curvature.

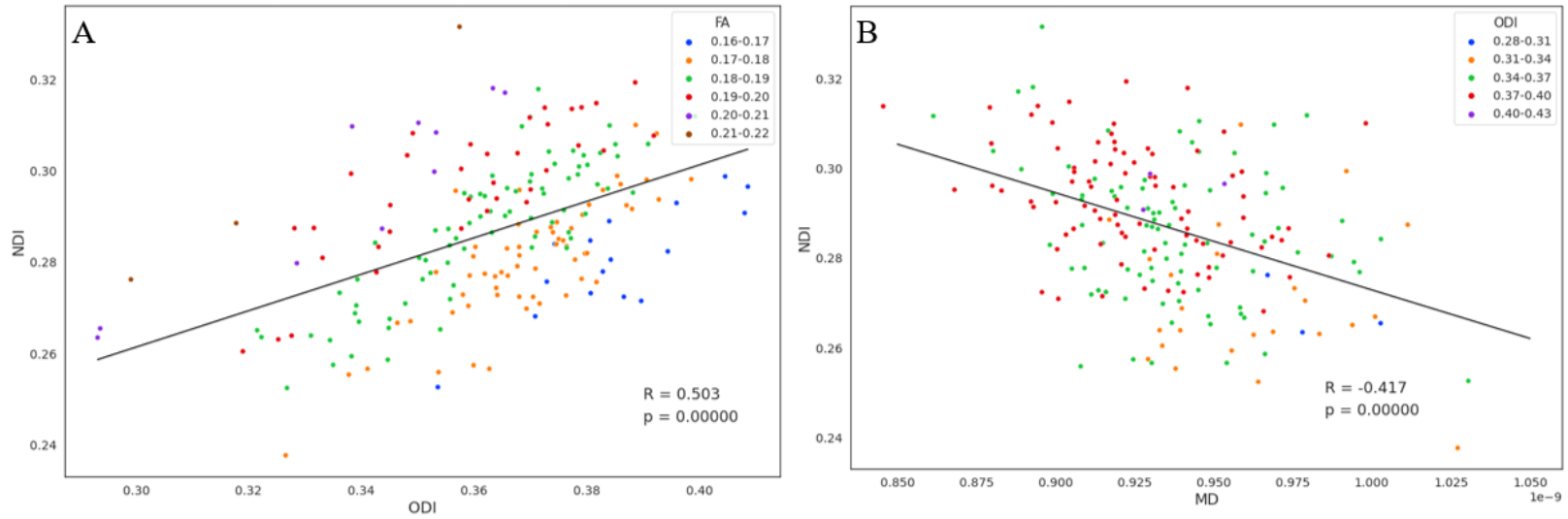

Supplementary Figure 2. Diffusion Tensor Imaging (DTI) metrics and their correlations with Neurite Orientation Dispersion and Density Imaging (NODDI) metrics. (A) Correlation between ODI and NDI grouped by ranges of FA values. (B) Correlation between MD and NDI grouped by ranges of ODI values.

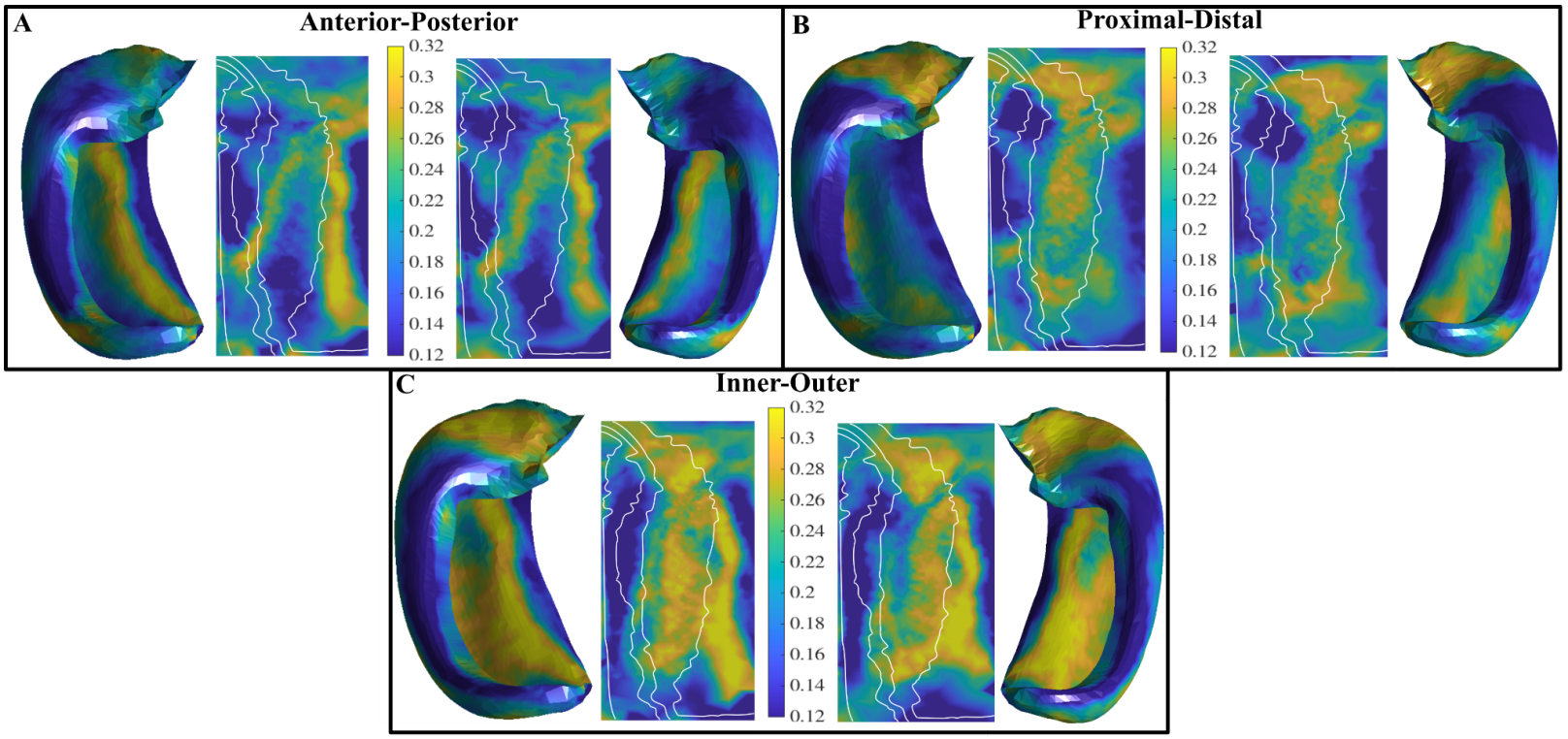

Supplementary Figure 3. Standard deviation of the cosine similarities between hippocampal axis vectors and NODDI vectors. Cosine similarities were sampled across the midthickness surface and are plotted on averaged surfaces.

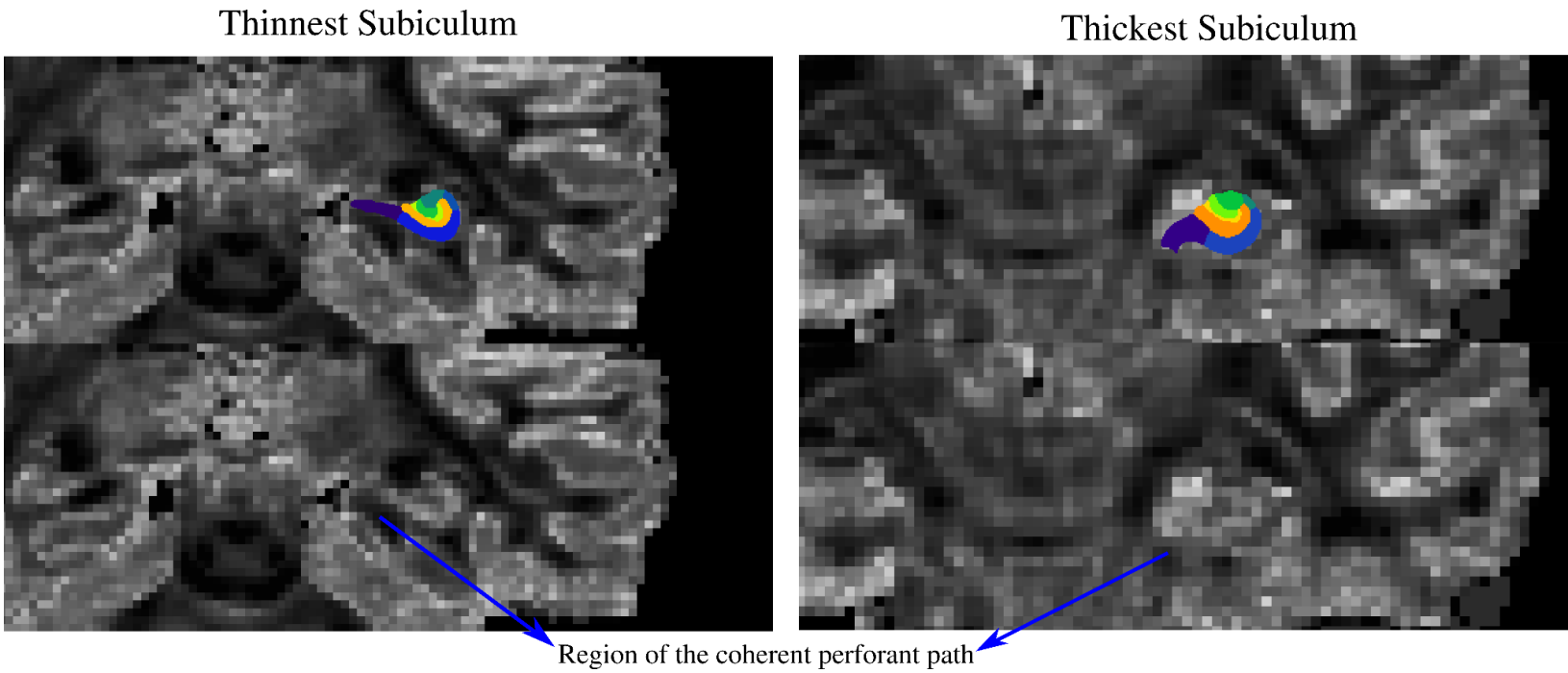

Supplementary Figure 4. Depicting the thinnest and thickest subiculum (purple subfield label) out of all 100 subjects plotted on top of the native space ODI image. Blue arrows point to regions of low dispersion which correspond to the highly coherent perforant path/angular bundle. Partial voluming can be seen with the thinnest subiculum, as lower ODI values from the perforant path/angular bundle are present in the gray matter. The thickest subiculum shows less partial voluming.

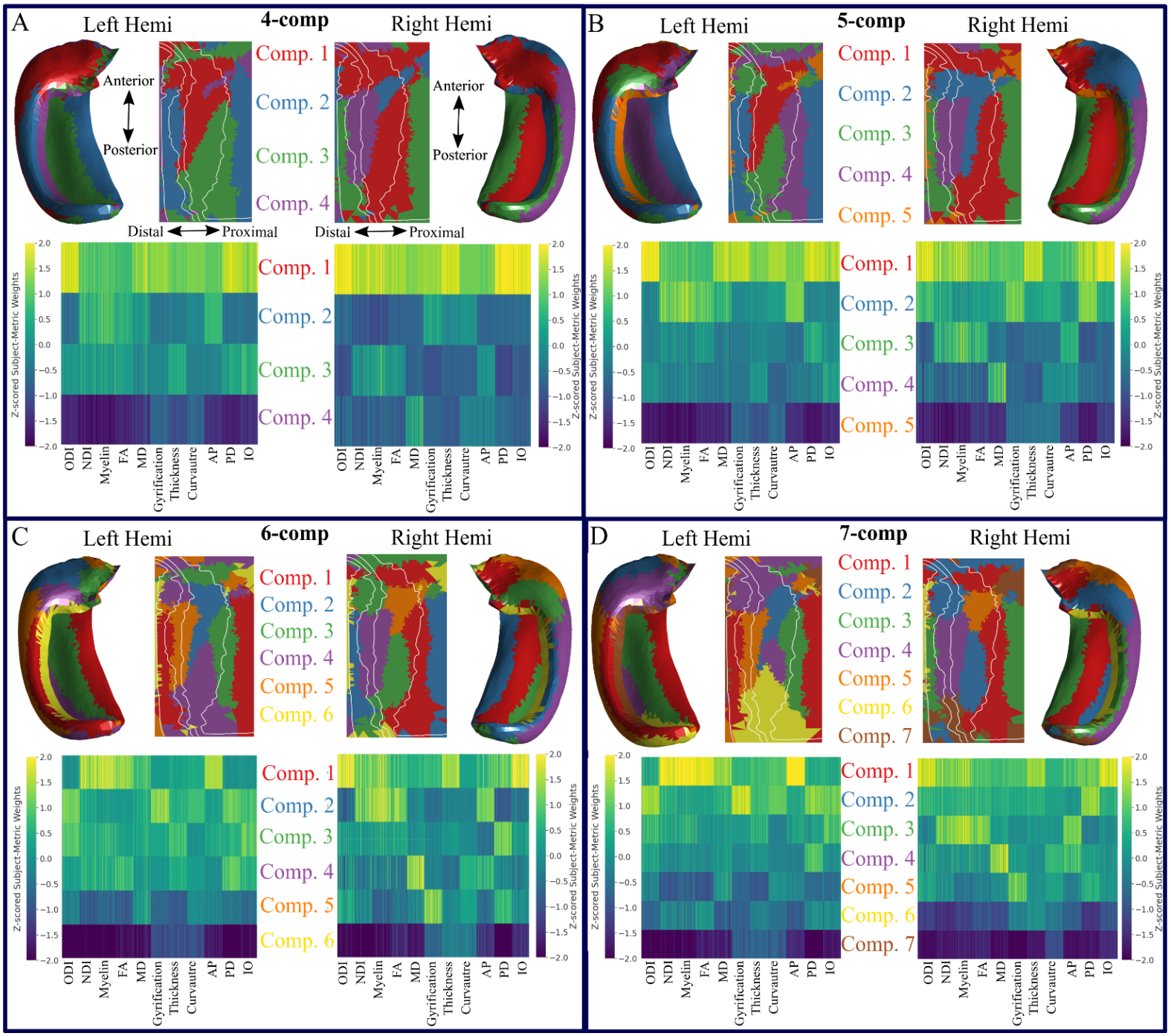

Supplementary figure 5. Varying the component value using all metrics for the NMF solution on the midthickness surface for left and right hippocampi. Winner-take all output at each vertex shown in folded and unfolded space at the top row of each box. White lines denote subfield borders. Bottom row in each box denotes the z-scored contribution of each metric for each component. (A) 4-component solution. (B) 5-component solution. (C) 6-component solution. (D) 7-component solution.

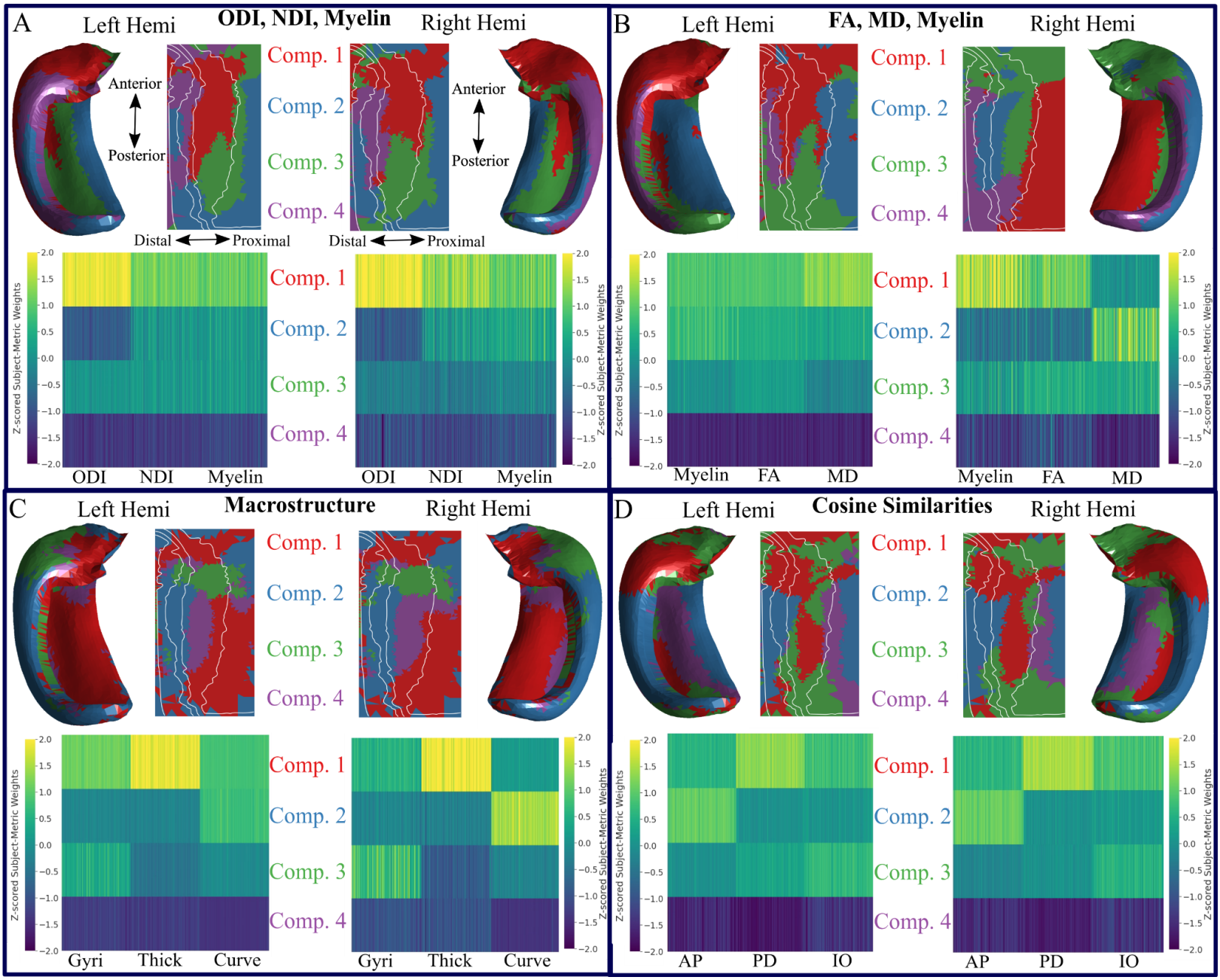

Supplementary figure 6. Varying the input metrics for the NMF solution on the midthickness surface for left and right hippocampi using a 4-component solution. Winner-take all output at each vertex is shown in folded and unfolded space at the top row of each box. White lines denote subfield borders. Bottom row in each box denotes the z-scored contribution of each metric for each component. (A) ODI, NDI, myelin input matrix. (B) FA, MD, myelin input matrix. (C) Macrostructure (gyrification, thickness, and curvature) input matrix. (D) Cosine similarity (AP, PD, and IO) input matrix.